



Contents lists available at ScienceDirect

Journal of Rock Mechanics and Geotechnical Engineering

journal homepage: www.jrmge.cn

Full Length Article

Parameter calibration of the tensile-shear interactive damage constitutive model for sandstone failure

Yun Shu^a, Zheming Zhu^b, Meng Wang^{b,c,*}, Weiting Gao^a, Fei Wang^a, Duanying Wan^a, Yuntao Wang^c

^a MOE Key Laboratory of Deep Earth Science and Engineering, College of Architecture and Environment, Sichuan University, Chengdu, 610065, China

^b Failure Mechanics and Engineering Disaster Prevention, Key Laboratory of Sichuan Province, Sichuan University, Chengdu, 610065, China

^c Tianfu Engineering-oriented Numerical Simulation & Software Innovation Center, Chengdu, 620107, China

ARTICLE INFO

Article history:

Received 12 February 2023

Received in revised form

17 May 2023

Accepted 14 August 2023

Available online 14 December 2023

Keywords:

Damage constitutive model

Parameter calibration

Rock modeling

Sandstone

Dynamic impact load

Tensile-shear interactive damage (TSID) model

ABSTRACT

The tensile-shear interactive damage (TSID) model is a novel and powerful constitutive model for rock-like materials. This study proposes a methodology to calibrate the TSID model parameters to simulate sandstone. The basic parameters of sandstone are determined through a series of static and dynamic tests, including uniaxial compression, Brazilian disc, triaxial compression under varying confining pressures, hydrostatic compression, and dynamic compression and tensile tests with a split Hopkinson pressure bar. Based on the sandstone test results from this study and previous research, a step-by-step procedure for parameter calibration is outlined, which accounts for the categories of the strength surface, equation of state (EOS), strain rate effect, and damage. The calibrated parameters are verified through numerical tests that correspond to the experimental loading conditions. Consistency between numerical results and experimental data indicates the precision and reliability of the calibrated parameters. The methodology presented in this study is scientifically sound, straightforward, and essential for improving the TSID model. Furthermore, it has the potential to contribute to other rock constitutive models, particularly new user-defined models.

© 2024 Institute of Rock and Soil Mechanics, Chinese Academy of Sciences. Production and hosting by Elsevier B.V. This is an open access article under the CC BY-NC-ND license (<http://creativecommons.org/licenses/by-nc-nd/4.0/>).

1. Introduction

Rocks extensively exist in underground drilling and rock excavation engineering. Rocks frequently undergo complex in situ stress and intense dynamic loads from blasting and earthquake wave (Zhang et al., 2021). Reliable safety design in related engineering requires careful and deep consideration of the complicated and diverse mechanics characteristics and failure modes of rocks under these loading conditions. Therefore, high-accuracy numerical simulation is an integral approach to reproducing these mechanical properties and failure processes. Numerical methods to model these phenomena include the finite element method (FEM) (Kuciewicz et al., 2020; Yang et al., 2020; Li et al., 2021a, 2021b), finite difference method (FDM) (Zhu et al., 2007, 2015; Wan et al.,

2019), material point method (MPM) (Wan et al., 2022), smooth particle hydrodynamics (SPH) (Xie et al., 2019; Gharehdash et al., 2020), discrete element method (DEM) (Jiang et al., 2015; Zhao et al., 2022), and peridynamics method (PDM) (Ying et al., 2022). Among the modeling methods, FEM is still the most frequently and universally used based on a frame of continuum mechanics. Irreversible plastic deformation and fracture can be reproduced by a damage evolution as a part of the constitutive models. The Holmquist-Johnson-Cook (HJC) model (Holmquist and Johnson, 2011), Johnson-Holmquist-Ceramic (JH2) model (Johnson and Holmquist, 1999), Riedel-Hiermaier-Thoma (RHT) model (Riedel et al., 1999), and Karagozian and Case (KC) model (Malvar et al., 1997) with different applicability are available in the FEM code such as LS-DYNA.

Both the HJC and JH2 models have two strength surfaces without the initial yield strength surface. The two models can capture the strain-rate effect, impact of pressure, and strain softening behavior. However, the tensile mechanical characteristics, influence of J_3 (the third invariant of the deviatoric stress), and strain hardening behavior cannot be reproduced. Thus,

* Corresponding author. Failure Mechanics and Engineering Disaster Prevention, Key Laboratory of Sichuan Province, Sichuan University, Chengdu, 610065, China.

E-mail address: wangmengscu@hotmail.com (M. Wang).

Peer review under responsibility of Institute of Rock and Soil Mechanics, Chinese Academy of Sciences.

modifications of the HJC and JH2 models have obtained great interest (Liu et al., 2020). The RHT and KC models have three failure surfaces considering three stress invariants. The difference is that the two models apply different plastic flow rules and damage evolution models. Consequently, in contrast to the KC model, the RHT model ignores the Lode-angle effect in the residual strength surface, shear dilation behavior, tension-compression asymmetry, and nonlinear characteristic of the move of the yield surface. The KC model employs a fractional-associative plastic flow rule and double-damage-variable definition for tension and shear. A damage scale factor is used to nonlinearly move the yield surface.

The technique of separately defining damage as a compressive/shear damage index and a tensile damage index has been developed for over two decades. Recent experimental results demonstrate that the influence of the hydrostatic pressure on tensile and shear damages should be considered (Cui et al., 2017). In addition, the degradation of the tensile strength after shear loads and decrease in shear strength after tensile loads cannot be precisely calculated because there is no interaction of tensile and shear damages. For the two problems, recently proposed rock constitutive models (Huang et al., 2021; Wang et al., 2021) primarily focus on improving the damage model by defining three damage indices: hydrostatic damage due to pore collapse, shear damage, and tensile damage. Nevertheless, the interaction of the tensile and shear damage due to tensile, shear, and hydrostatic loads has not been quantitatively described (Shu et al., 2022).

Based on the MKF model of Wang et al. (2021) and KC model, a new tensile-shear interactive damage (TSID) model was presented for the hydrostatic pressure-induced damage and the interaction of tensile and shear damages under impact and blast loads (Shu et al., 2022). The TSID model includes three invariants and three smooth failure surfaces. The damage evolution formulae of the TSID model were established based on Mohr-Coulomb criterion to quantitatively analyze the effects of the shear load on the tensile strength and tensile load on the shear strength. In the TSID model, the volumetric behavior and its resulting decreases in tensile and shear strengths from the hydrostatic pressure were explained as the tensile and shear damages caused by the hydrostatic pressure. The hydrostatic pressure-induced tensile and shear damages were coupled into the damage model based on several empirical equations from previous test data (Cui et al., 2017).

Although the TSID model has been validated from the element scale to the experimental specimen scale and from the quasi-static loading rate to the high-strain-rate condition, several local problems remain to be resolved, such as the linearization of the relationships between maximum strength surface and initial yield strength surface and between maximum strength surface and residual strength surface when $p \geq f_c/3$. Other modifications will be discussed in Section 2. In addition, the calibrating method of undetermined parameters was not sufficiently detailed and clear in the original TSID model (Shu et al., 2022). The model has over 30 uncertain parameters, which can be divided into four types: strength model, equation of state (EOS), strain-rate effect, and damage evolution formulae.

For a more precise and profound insight into the parameter calibration procedure, the undetermined parameters can be classified into two categories: parameters that are directly or indirectly determined by experiments and parameters that are determined using the numerical trial-and-error method. For the first type of parameters, a fundamental issue is how to specify the parameter when the related experiment requirement is too difficult to conduct due to limited experimental conditions. Significantly, as the critical pressure of the compacted stages, the lock pressure in

an EOS usually exceeds 0.5 GPa, which is beyond the maximum loading capacity of most common triaxial loading devices. For the other type of parameters, in the numerical trial-and-error method, the control variate method can be used to separately determine each parameter. Then, a crucial issue is the order of the undetermined parameters for the control variate method, which should be seriously considered based on the insight for the function and relation of the parameters.

In this paper, sandstone from Neijiang City of China was taken as an example to show a calibration procedure of the TSID model parameters. First, the original TSID model is described with local modifications, and the model is implemented in LS-DYNA. Then, the sandstone is used to conduct a series of static and dynamic tests to acquire general mechanical parameters. Next, a detailed calibration procedure for the TSID model parameters of the sandstone is elaborated based on the sandstone test results from this paper and previous research. Each parameter is determined according to the order of the strength surface, EOS, strain rate effect, and damage-related parameters. Numerical tests of unconfined uniaxial compression (UUC), triaxial compression (TXC), and Brazilian disc (BD) are conducted to evaluate the basic performance of the calibrated parameters for quasi-static loading conditions. Finally, the dynamic performance of the calibrated parameters is validated by simulating SHPB Brazilian disc and compression tests. A scientific and clear parameter calibration method will significantly help the TSID model to be more widely applied. In addition, the forming process of the parameter calibration method in this paper is appropriate for the TSID model and contributes to other rock constitutive models.

2. Description of the TSID model

The TSID model was recently proposed with powerful ability for rock-like materials, especially under dynamic loads (Shu et al., 2022). The TSID model has three invariants and three smooth failure strength surfaces. In addition to common mechanical behaviors such as the strain-rate effect, pressure dependency, tension-compression asymmetry, Lode-angle effect, shear dilation, strain hardening, and strain softening, the TSID model focuses on the hydrostatic-pressure-induced damage and interaction of tensile and shear damages.

Compared with other models such as KC, KF (Kong et al., 2018) and the model of Yang (Yang et al., 2020), the original TSID model has advantages in five aspects: (i) The effects of the tensile load on the shear damage and shear load on the tensile damage can be accurately calculated; (ii) The effect of the hydrostatic load on the tensile and shear damages is involved; (iii) The tension-compression asymmetries of the damage evolution and strain-rate effect are considered in the original TSID model; (iv) The piecewise strength surfaces used by the existing models are not smooth, which may lead to convergence problems, while the TSID model overcomes this problem; and (v) A new expression of the damage scale factor $\eta(\lambda)$ with greater efficiency is adopted.

Herein, the original TSID model has been slightly modified including: (i) The maximum failure strength surface and residual strength surface are separately defined instead of being proportional to each other as in the original TSID model; (ii) The nonlinear characteristics of the relation between pressure and volume cannot be simultaneously and precisely described by the cubic polynomial EOS in the original TSID model, so a linear equation in the low-pressure region is added herein; (iii) The strain-rate effect commonly exhibits a highly non-symmetrical increase rate under tensile and compressive loads, which should be separately defined

according to tension and compression; and (iv) The damage parameter r_{conf} is redefined to determine the parameters.

2.1. Strength model

Fig. 1 shows a typical stress-strain curve under uniaxial tensile and compressive loads. The material undergoes an elastic stage before achieving the yield strength f_{yt} or f_{yc} , followed by the strain hardening until the peak failure strength f_t or f_c . After the peak strength, the material enters the strain softening stage.

The TSID model has three strength surfaces: an initial yield strength surface (σ_y), a maximum failure strength surface (σ_m), and a residual strength surface (σ_r), as illustrated in Fig. 2a. σ_m is located by the triaxial tensile strength ($-T, 0$), uniaxial tensile strength $A(-f_t/3, f_t)$, pure shear strength $B(0, 3f_t)$, and uniaxial compressive strength $C(f_c/3, f_c)$. Similarly, the triaxial tensile yield strength ($-T_y, 0$), uniaxial tensile yield strength $A_y(-f_{yt}/3, f_{yt})$, pure shear yield strength $B_y(0, 3f_{yt})$, and uniaxial compressive yield strength $C_y(f_{yc}/3, f_{yc})$ are used to locate σ_y . Generally, it is difficult to determine f_{yt} from the tensile stress-strain curve. Herein, f_{yt} is given by supposing $3f_{yt}/(3f_t) = f_{yc}/f_c$ as recommended by Wang et al. (2021).

Both σ_m and σ_y consist of three piecewise functions with equal derivatives at the connecting points (A, B, C, A_y, B_y , and C_y) to ensure smoothness. σ_m , σ_y , and σ_r are defined as follows:

$$\sigma_m = \begin{cases} \sigma_{m1} = \frac{p+T}{a_{1m1}+a_{2m1}p} & (p < 0) \\ \sigma_{m2} = \frac{p}{a_{1m2}+a_{2m2}p} + 3f_t & (0 \leq p < \frac{f_c}{3}) \\ \sigma_{m3} = \frac{p}{a_{1m3}+a_{2m3}p} + a_{0m3} & (p \geq \frac{f_c}{3}) \end{cases} \quad (1)$$

$$\sigma_y = \begin{cases} \sigma_{y1} = \frac{p+T_y}{a_{1y1}+a_{2y1}p} & (p < 0) \\ \sigma_{y2} = \frac{p}{a_{1y2}+a_{2y2}p} + 3f_{yt} & (0 \leq p < \frac{f_{yc}}{3}) \\ \sigma_{y3} = \left[\frac{p}{a_{1y3}+a_{2y3}p} + a_{0y3} \right] f_{\text{cap}}(p) = \left[\frac{p}{a_{1y3}+a_{2y3}p} + a_{0y3} \right] \sqrt{1 - \left(\frac{p - \frac{f_{yc}}{3}}{p_{\text{close}} - \frac{f_{yc}}{3}} \right)^2} & (p \geq \frac{f_{yc}}{3}) \end{cases} \quad (2)$$

$$\sigma_r = \frac{p}{a_{1r} + a_{2r}p} \quad (3)$$

where p is the hydrostatic pressure; $T, a_{1m1}, a_{2m1}, a_{1m2}, a_{2m2}, a_{1m3}, a_{2m3}$, and a_{0m3} are the σ_m -related parameters. Among them, only the σ_{m3} -related parameters a_{1m3}, a_{2m3} , and a_{0m3} should be determined according to conventional TXC test results under different confining pressures; the other five parameters can be obtained using the smooth continuity condition.

The σ_y -related parameters are similar to σ_m , but a cap function $f_{\text{cap}}(p)$ was introduced into σ_{y3} to weaken the yield strength of rock-like materials under high pressure. The parameter p_{close} is the pressure where the initial yield strength is nearly zero.

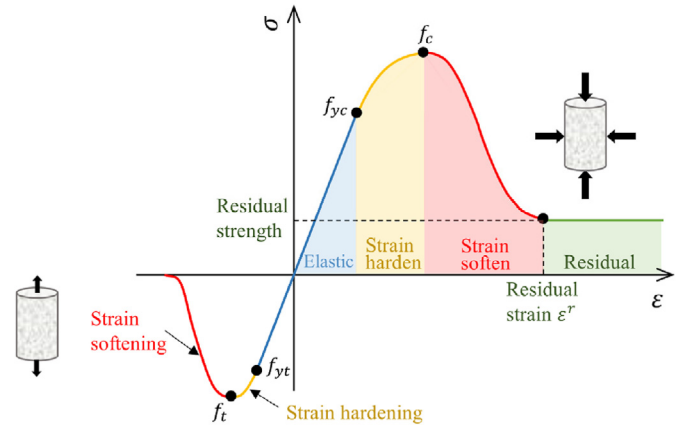


Fig. 1. Schematic diagram of the typical stress-strain relationship of rock-like materials.

The σ_r -related parameters a_{1r} and a_{2r} should also be given by TXC tests.

The current yield surface (σ_y) migrates from σ_y to σ_m in the strain hardening stage and subsequently drops from σ_m to σ_r in the strain softening stage. To capture the nonlinear characteristics of strain hardening and softening, a damage scale factor $\eta(\lambda)$ was employed to connect σ_y with the current damage λ as follows:

$$\sigma_Y = \begin{cases} r(\theta, \varphi) [(1-\eta)\sigma_y + \eta\sigma_m] & (\lambda \leq \lambda_m, \eta \text{ from } 0 \text{ to } 1, \text{ hardening}) \\ r(\theta, \varphi) [(1-\eta)\sigma_r + \eta\sigma_m] & (\lambda > \lambda_m, \eta \text{ from } 1 \text{ to } 0, \text{ softening}) \end{cases} \quad (4)$$

where λ_m is equal to λ when $\eta = 1$, which is a user-defined parameter. When λ increases from 0 to λ_m , strain hardening occurs, while η varies from 0 to 1. Then, λ continues to increase from

λ_m , which indicates strain softening, while η decreases from 1 to 0, followed by retaining at the residual surface. The detail about $\eta(\lambda)$ is shown in Section 2.4 for the damage model.

$r(\theta, \varphi)$ in Eq. (4) is a shape function adapted to describe the effect of the third invariant on the shape of the current yield surface. The shape of the yield surface on the meridian plane for rock-like materials gradually varies from triangular under low pressure to circular under high pressure. $r(\theta, \varphi)$ can be given as (Liu et al., 2020):

$$r(\theta, \varphi) = \frac{2(1-\varphi^2)\cos\theta + (2\varphi-1)\sqrt{4(1-\varphi^2)\cos^2\theta + 5\varphi^2 - 4\varphi}}{4(1-\varphi^2)\cos^2\theta + (1-2\varphi)^2} \quad (5)$$

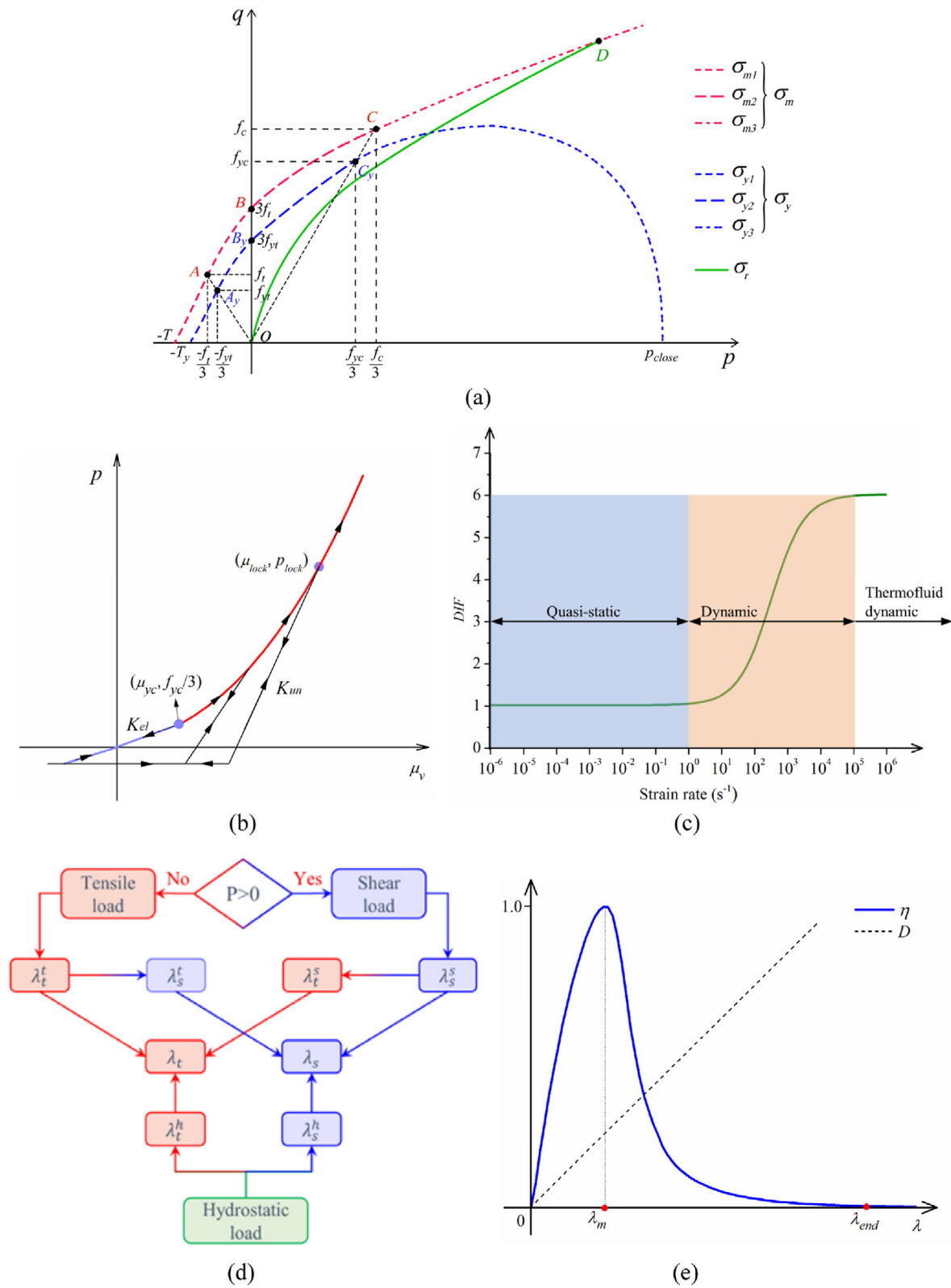


Fig. 2. TSID model: (a) Strength model, (b) EOS, (c) Strain rate effect, (d) Damage model, and (e) Damage scale factor η .

$$\cos(3\theta) = \frac{27J_3}{2\sigma_{eq}^3}$$

$$(6) \quad \sigma_{eq} = \sqrt{\frac{3}{2} s_{ij} s_{ij}} \quad (7)$$

where θ is the Lode angle; J_3 is the third invariant of the deviatoric stress tensor; σ_{eq} is the equivalent stress; s_{ij} is the deviatoric stress tensor; and φ is the tensile-to-compressive meridian ratio, which can be determined as (Polanco-Loria et al., 2008; Liu et al., 2020):

$$\varphi = \begin{cases} 0.65 & (p_{nor} < 0) \\ 0.65 + (1 - 0.65) \frac{p_{nor}}{10} & (0 \leq p_{nor} \leq 10) \\ 1 & (p_{nor} \geq 10) \end{cases} \quad (8)$$

where p_{nor} is the normalized pressure, and $p_{nor} = p/f_c$.

2.2. Equation of state (EOS)

An appropriate EOS should be defined to describe the relationship between hydrostatic pressure p and volumetric strain μ_v . In the EOS of the TSID model for compression, the material will undergo three stages: elastic, compacting, and compacted stages, as shown in Fig. 2b. The elastic stage is a straight line with an end at the uniaxial compressive yield strength point ($\mu_{yc}, f_{yc}/3$). For the loading condition of the compacting and compacted stages, the hydrostatic pressure is as follows:

$$p(\mu_v) = \begin{cases} K_{el}\mu_v & \left(p < \frac{f_{yc}}{3}\right) \\ K_1\mu_v + K_2\mu_v^2 + K_3\mu_v^3 & \left(p \geq \frac{f_{yc}}{3}\right) \end{cases} \quad (9)$$

where K_{el} is the unloading bulk modulus in the linear elastic region; and K_1 , K_2 , and K_3 are the parameters determined by experimental data.

When the material is under unloading or reloading conditions, as shown in Fig. 2b, the following incremental form can be used:

$$\Delta p = \Delta\mu_v K_{UN} \quad (10)$$

where K_{UN} is the unloading or reloading bulk modulus, which can be given as

$$K_{UN} = \begin{cases} K_{el} & \left(p < p_{yc} = \frac{f_{yc}}{3}\right) \\ (1 - \lambda_{com})K_{el} + \lambda_{com}K_{lock} & (p_{yc} \leq p \leq p_{lock}) \\ K_{lock} & (p > p_{lock} = p(\mu_{lock})) \end{cases} \quad (11)$$

$$\lambda_{com} = \frac{\mu_v - \mu_{yc}}{\mu_{lock} - \mu_{yc}} \quad (12)$$

where K_{lock} is the unloading bulk modulus in the linear elastic and compacted regions; and λ_{com} is the linear interpolation factor to calculate K_{UN} , which linearly increases from K_{el} to K_{lock} when $p_{yc} \leq p \leq p_{lock}$.

2.3. Strain-rate effect

To accurately capture the compressive or tensile strength growth with strain rate under dynamic loads, as shown in Fig. 2c, a dynamic increase factor (DIF) was widely employed as follows (Gebben and Ruppert, 2000; Xu and Wen, 2016; Liu et al., 2020; Yang et al., 2020):

$$DIF_t = \frac{f_{td}}{f_t} = \left\{ \left\{ \tanh \left[\log_{10} \left(\frac{\dot{\epsilon}}{\dot{\epsilon}_0} \right) - W_x \right] S \right\} \left(\frac{F_m}{W_y} - 1 \right) + 1 \right\} W_y \quad (13)$$

$$DIF_s = \frac{f_{cd}}{f_c} = \frac{f_t}{f_c} (DIF_t - 1) + 1 \quad (14)$$

where f_{td} and f_{cd} are the dynamic f_t and f_c , respectively; $\dot{\epsilon}_0 = 1$ is the reference strain rate; and W_x , W_y , F_m , and S are the fitting parameters from tests.

The strain rate effect described by Eqs. (13) and (14) has two problems. The first is that the function of each parameter in Eq. (13) is not sufficiently clear. Hence, Eq. (13) should be improved for more specific physics significance of the four parameters in Eq. (13), as follows:

$$DIF_t = \frac{f_{td}}{f_t} = \frac{DIF_{max}^t + 1.01}{2} + \frac{DIF_{max}^t - 1}{2} \tanh \left[V_x^t \log_{10} \left(\frac{\dot{\epsilon}}{\dot{\epsilon}_0} \right) - V_y^t \right] \quad (15)$$

where V_x^t , V_y^t , and DIF_{max}^t will be determined from the dynamic SHPB split test results.

Eq. (15) is established based on the transformation of Eq. (13). However, Eq. (15) has fewer undetermined parameters than Eq. (13). In addition, each parameter of Eq. (15) has its specific physics significance, which is elaborated in Section 4.3.

The second problem is that the fixed proportional relationship between DIF_t and DIF_s , as shown in Eq. (14), is not supported by existing experimental data. DIF commonly exhibits a highly non-symmetrical increase rate under tensile and compressive loads. If sufficient dynamic compression test data are available, a more accurate dynamic compressive (shear) strength can be predicted by fitting the dynamic compressive test data instead of the fixed proportional relationship of Eq. (14). Thus, DIF_t and DIF_s should be separately defined according to the tension and compression, respectively, based on dynamic test results. DIF_s herein is defined as

$$DIF_s = \frac{f_{cd}}{f_c} = \frac{DIF_{max}^s + 1.01}{2} + \frac{DIF_{max}^s - 1}{2} \tanh \left[V_x^s \log_{10} \left(\frac{\dot{\epsilon}}{\dot{\epsilon}_0} \right) - V_y^s \right] \quad (16)$$

where V_x^s , V_y^s , and DIF_{max}^s will be determined from dynamic SHPB compression test results.

Most dynamic experiments were conducted using uniaxial tests, and the stress path on the meridian is radial from the origin. Thus, the “radial enhancement approach” recommended by KC, RHT, and KF models is adopted (Kong et al., 2018):

$$\sigma_Y = DIF \sigma_Y \left(\frac{p}{DIF} \right) \quad (17)$$

2.4. Damage model

In the TSID model, the tensile damage index λ_t and shear damage index λ_s are independently defined and originate from three load sources: tensile load, shear load, and hydrostatic load, as illustrated in Fig. 2d:

$$\lambda_t = \lambda_t^t + \lambda_t^s + \lambda_t^h \quad (18)$$

$$\lambda_s = \lambda_s^s + \lambda_s^t + \lambda_s^h \quad (19)$$

where λ_t^t is the tensile load-induced tensile damage, λ_s^s is the shear load-induced tensile damage, λ_t^h is the hydrostatic load-induced tensile damage, λ_s^s is the shear load-induced shear damage, λ_s^t is the tensile load-induced shear damage, and λ_s^h is the hydrostatic load-induced shear damage.

λ_t^t and λ_s^s are defined as

$$\left. \begin{aligned} \lambda_t^t &= \frac{\sum \Delta \epsilon_1^p}{DIF_t \left(1 + \frac{|p|}{DIF_{ft}}\right)^{b_1}} \quad (p < 0) \\ \lambda_s^s &= \frac{\sum \Delta \epsilon_{eq}^p}{DIF_s \left(1 + \frac{p}{DIF_{fs}}\right)^{b_2}} \quad (p \geq 0) \end{aligned} \right\} \quad (20)$$

where $\Delta \epsilon_1^p$ is the maximum principal component of plastic strain increment, $\Delta \epsilon_{eq}^p$ is the increment of the equivalent plastic strain, b_1 and b_2 are the damage constants that govern the increase rate of the damage index with plastic strain.

Combining with Mohr-Coulomb criterion, λ_t^s and λ_s^t , as the interaction parts between tensile and shear damages, can be expressed as (Shu et al., 2022):

$$\left. \begin{aligned} \lambda_t^s &= (1 - \lambda_t) \lambda_s^s \\ \lambda_s^t &= (1 - \lambda_s) \frac{\sigma_Y|_{p=0}}{\sigma_Y} \lambda_t^t \end{aligned} \right\} \quad (21)$$

A more detailed derivation process of Eq. (21) can be found in our previous work (Shu et al., 2022), which is not elaborated herein.

Under a high hydrostatic load, tensile and shear damage will be generated around the collapsed pores or voids according to a recent report (Cui et al., 2017). λ_t^h can be expressed as the product of the undamaged proportion $(1 - \lambda_t)$, strength reduction proportion $(1 - r_t)$, and a confining factor r_{conf} , which is similar to λ_s^h :

$$\left. \begin{aligned} \lambda_t^h &= (1 - \lambda_t)(1 - r_t)r_{conf} \\ \lambda_s^h &= (1 - \lambda_s)(1 - r_s)r_{conf} \end{aligned} \right\} \quad (22)$$

where r_t and r_s are the residual ratios of the unconfined uniaxial tensile (UUT) and UUC strengths, respectively, after the effect of different hydrostatic pressures. According to the experimental results (Cui et al., 2017), r_t and r_s are

$$\left. \begin{aligned} r_t &= \frac{f_t^h}{f_t} = \left(\frac{p_{max}}{PtFf_c}\right)^{R_t^h} \\ r_s &= r_c = \frac{f_c^h}{f_c} = 1 - R_s^h \ln\left(\frac{p_{max}}{PtFf_c}\right) \end{aligned} \right\} \quad (p_{max} > PtFf_c) \quad (23)$$

where f_t^h and f_c^h are the residual UUT strength and residual UUC strength after the effect of the maximum hydrostatic pressure p_{max} , PtF governs the threshold of the hydrostatic pressure to start considering hydrostatic-pressure-induced damage, and R_t^h and R_s^h are the fitting parameters determined by test data.

r_{conf} is the confining factor to estimate the current effectivity of the hydrostatic compressive state (Kong et al., 2018; Pereira et al., 2018; Yang et al., 2020). When the material enters the tensile or shear yield stage, the hydrostatic compressive state can be ignored, and the hydrostatic pressure-induced damages are set to zero. r_{conf} can be given as

$$r_{conf} = 1 - \frac{\sqrt{3}J_2}{\sigma_Y(p)} = \begin{cases} 0 & (\sqrt{3}J_2 \geq \sigma_Y(p)) \\ 1 - \frac{\sqrt{3}J_2}{\sigma_Y(p)} & (\sqrt{3}J_2 < \sigma_Y(p)) \end{cases} \quad (24)$$

where $\sigma_Y(p)$ is the initial yield strength.

After the damage has been obtained, the damage scale factor $\eta(\lambda)$ can be calculated to locate the current yield surface:

$$\eta(\lambda) = \begin{cases} \eta_t = \frac{e^{-\alpha_t \lambda_t} - e^{-\beta_t \lambda_t}}{e^{-\alpha_t \lambda_m^t} - e^{-\beta_t \lambda_m^t}} & (p < 0) \\ \eta_s = \frac{e^{-\alpha_s \lambda_s} - e^{-\beta_s \lambda_s}}{e^{-\alpha_s \lambda_m^s} - e^{-\beta_s \lambda_m^s}} & (p \geq 0) \end{cases} \quad (25)$$

Let $i = t$ for tension and $i = s$ for shear, α_i and β_i can be given after determining β_i/α_i and λ_m^i :

$$\left. \begin{aligned} \alpha_i &= \frac{\ln\left(\frac{\beta_i}{\alpha_i}\right)}{\lambda_m^i} \\ \beta_i &= \left(\frac{\beta_i}{\alpha_i}\right) \alpha_i \\ BtA_i &= \beta_i/\alpha_i \end{aligned} \right\} \quad (26)$$

The hardening and softening rates are controlled by λ_m^i and tA_i , respectively, as shown in Fig. 2e.

The ratio of the softening range to the hardening range can be approximately calculated by (Shu et al., 2022):

$$\frac{\lambda_{end}}{\lambda_m} = 2\beta/\alpha + 4 \quad (27)$$

For the convenience of post-processing, normalized damage variables of D_t and D_s , which vary from 0 to 1, must be introduced as follows:

$$\left. \begin{aligned} D_t &= \min\left(\frac{\lambda_t}{\lambda_{end}^t}, 1\right) \\ D_s &= \min\left(\frac{\lambda_s}{\lambda_{end}^s}, 1\right) \end{aligned} \right\} \quad (28)$$

where λ_{end}^t and λ_{end}^s are equal to λ_{end} in tension and shear, respectively.

As the normalized damage variables, D_t and D_s are introduced to only illustrate the damage level (as Fig. 2e) but not used in the subsequent calculation process. Similarly, D_t^t , D_t^s , D_t^h , D_s^s , D_s^t , and D_s^h respond to the above λ_t^t , λ_t^s , λ_t^h , λ_s^s , λ_s^t , and λ_s^h , respectively. If there is no special declaration, the following “damage” defaults to the normalized damage variables.

3. General mechanical parameters of the sandstone specimen

Sandstone is a common sedimentary rock. The sandstone in this paper was taken from Neijiang City of Sichuan Province in China with good homogeneity. To ensure the consistence of mechanical properties of the sandstone, all specimens were cut from a complete rock. The sandstone mainly comprised approximately 47% quartz, 27% feldspar, 15% debris, 1% mica, and 1% opaque minerals.

A series of static and dynamic tests was performed according to the rock test procedure recommended by ISRM (International Society for Rock Mechanics). Static tests include UUC tests, BD tests,

TXC tests, and hydrostatic compression (HYC) tests. Dynamic tests were conducted with a split Hopkinson pressure bar (SHPB) device, including SHPB compression and SHPB Brazilian disc tests.

The samples for the UUC, TXC, and HYC tests were cylinders with a 2:1 height/diameter ratio (100 mm/50 mm). Specimens with a 1:1 depth/diameter ratio (50 mm/50 mm) were selected for the SHPB compression tests. The sandstone for the static and dynamic Brazilian tests was processed into a disc with a 1:2 depth/diameter ratio (25 mm/50 mm).

UUC and BD tests were performed using a compression test machine with the displacement control method at a loading rate of 1.2 mm/min, as shown in Fig. 3a. TXC tests under confining pressures of 5 MPa, 10 MPa, 20 MPa, and 30 MPa were conducted on an MTS-815 servo-controlled testing system at Sichuan University, as shown in Fig. 3b. The sample was axially loaded by a solid piston after hydrostatic pressure had been applied by pressurized oil to a specified confining pressure. The confining pressure was loaded at a rate of 4 MPa/min, while the axial load was applied at a rate of 0.1 mm/min.

Dynamic tests were performed with a $\phi 75$ mm SHPB system, as shown in Fig. 3c. The test device consisted of a striker (0.4 m long), an incident bar (3 m long), a transmission bar (2 m long), and a momentum bar. The bars and striker were 75 mm in diameter and had an elastic modulus of 210 GPa. A high-speed camera was used to capture transient fracture images. A cupreous wave shaper was employed to optimize the loading waves. The stress wave on the incident and transmission bars was captured by two strain gages, converted into a voltage signal to be processed through the oscilloscope (DS1000Z-E) and high dynamic-strain indicator (CS-1A) (Gao et al., 2022).

The test method is not illustrated in detail here, but other information about the tests is shown in Section 5. The experimental results of the UUC and BD tests were averaged (data with deviations over 30% were ignored), as presented in Fig. 4 and Tables 1–3. The tensile strength f_{BD} of BD tests is commonly approximately 15% smaller than the uniaxial tensile strength f_t from direct tension tests, thus $f_t = 1.15f_{BD}$ was adopted, as recommended by Pittet and Lemaitre (2000) and Kuciewicz et al. (2021).

4. Determination of the TSID model parameters

In total, 37 parameters must be determined in the TSID model. Most of them can be obtained by experiments, several parameters should be determined using the numerical trial-and-error method, and the others should be calculated based on the prior determined parameters. In addition to the basic parameters measured in Table 1, the undetermined parameters can be classified into four categories: strength-model-related parameters, EOS parameters, strain-rate effect parameters, and damage-model-related parameters. The four types of parameters should be calibrated using the following procedure.

4.1. Calibration of failure strength surfaces

As introduced in Section 2.1, the TSID model involves three strength surfaces: the initial yield strength surface (σ_y), maximum failure strength surface (σ_m), and residual strength surface (σ_r). Except for σ_r , σ_m and σ_y are composed of three piecewise functions. The parameters related to σ_{m3} , σ_{y3} , and σ_r must be calibrated using TXC test data. This paper involves the TXC test results (Table 2) under low confining pressure. Nonetheless, the data for high confining pressure come from previous research, where the samples were also sandstone with a similar compressive strength to that in this paper.

4.1.1. Determination of σ_{m3} , σ_{y3} , and σ_r

As depicted in Fig. 5d, the UUC strength ($f_c/3$, f_c) is the fixed origin of σ_{m3} :

$$\sigma_{m3} \left(\frac{f_c}{3} \right) = \frac{\left(\frac{f_c}{3} \right)}{a_{1m3} + a_{2m3} \left(\frac{f_c}{3} \right)} + a_{0m3} = f_c \quad (29)$$

Thus, only a_{1m3} and a_{2m3} must be calibrated using a set of TXC test results. Many compressive peak strength values under different confining pressures were collected from this paper and previous

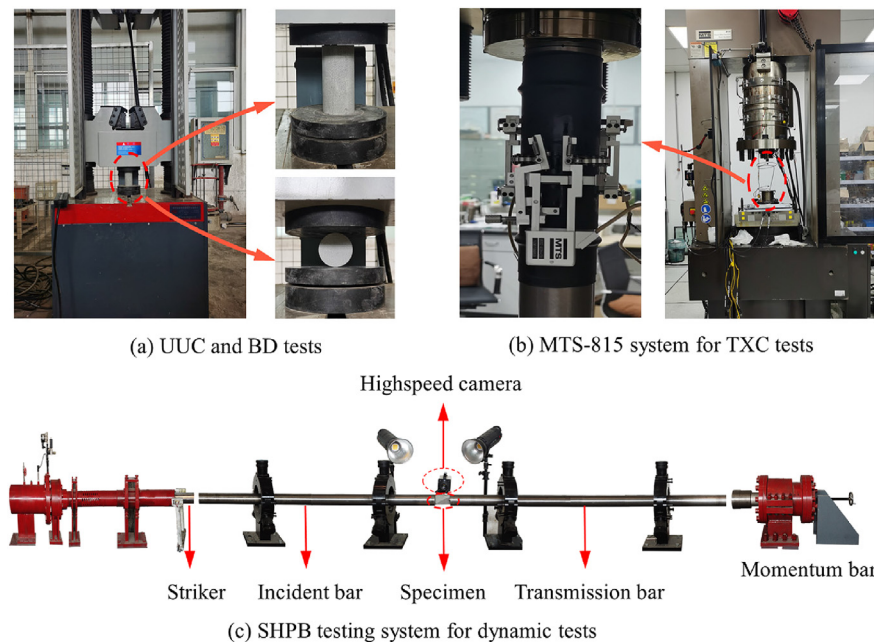


Fig. 3. Test devices for the (a) UUC and BD tests; (b) TXC tests at confining pressures of 5 MPa, 10 MPa, 20 MPa, and 30 MPa; and (c) dynamic tests with the SHPB system.

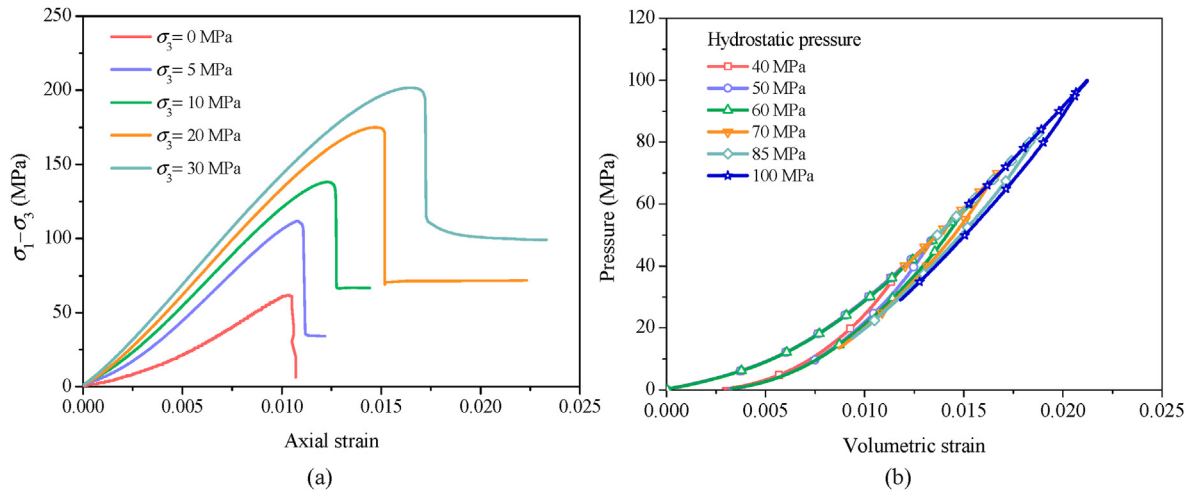


Fig. 4. Experimental results: (a) UUC and TXC tests and (b) hydrostatic compressive tests under different hydrostatic pressures.

Table 1

Basic parameters of the sandstone.

Density, ρ (g/ cm ³)	Elastic modulus, E (GPa)	Poisson's ratio, ν	Uniaxial compressive strength (UCS), f_c (MPa)	BD tensile strength, f_{BD} (MPa)	Uniaxial tensile strength (UTS), f_t (MPa)
2.6	5.94	0.2	61.2	5.07	5.83

reports (Gowd and Rummel, 1980; Ayling et al., 1995; Zong et al., 2016), as listed in Fig. 5a, with the fitting result of the equation of σ_{m3} . Then, a_{0m3} can be obtained using Eq. (29). The values of a_{0m3} , a_{1m3} and a_{2m3} are determined as

$$\left. \begin{aligned} a_{0m3} &= 19.77 \text{ MPa} \\ a_{1m3} &= 0.4469 \\ a_{2m3} &= 0.05504/f_c = 8.994 \times 10^{-4} \text{ MPa}^{-1} \end{aligned} \right\} \quad (30)$$

Then, σ_{m3} is written as

$$\sigma_{m3} = \frac{p}{0.4769 + \left(\frac{0.0465}{f_c}\right)p} + 19.77 \text{ MPa} \quad \left(p > \frac{f_c}{3}\right) \quad (31)$$

Similar to σ_{m3} , the parameters related to σ_{y3} can be determined from the fitting result of the yield strengths under different pressures measured by this paper and previous reports (Gowd and Rummel, 1980; Ayling et al., 1995; Zong et al., 2016), as shown in Fig. 5b:

Table 2

UUC and TXC test results to determine the strength-model-related parameters.

$\sigma_2 = \sigma_3$ (MPa)	Maximum strength, f^m (MPa)	Yield strength, f^y (MPa)	Residual strength, f^r (MPa)	Axial strain at peak, ϵ^m	Axial strain at yield, ϵ^y	Average modulus before yield, \bar{E} (GPa)
0	61.2	55.8		0.0104	0.0094	5.94
5	111.78	98	34.12	0.0108	0.00923	10.63
10	138	108	66.7	0.01237	0.00892	12.1
20	175.1	132.7	70	0.01474	0.00999	13.28
30	201.7	145	99.1	0.01646	0.01053	13.77

$$\left. \begin{aligned} a_{0y3} &= 18.62 \text{ MPa} \\ a_{1y3} &= 0.475 \\ a_{2y3} &= \frac{0.0759}{f_{yc}} = 1.36 \times 10^{-3} \text{ MPa}^{-1} \\ p_{\text{close}} &= 424.6 \text{ MPa} \end{aligned} \right\} \quad (32)$$

Thus, σ_{y3} can be determined as

$$\sigma_{y3} = \left[\frac{p}{0.434 + \left(\frac{0.063}{f_{yc}}\right)p} + 11.231 \right] \sqrt{1 - \left(\frac{p - \frac{f_{yc}}{3}}{436.3 - \frac{f_{yc}}{3}}\right)^2} \quad \left(p > \frac{f_{yc}}{3}\right) \quad (33)$$

σ_r was calibrated by fitting many residual strength values of sandstone (Gowd and Rummel, 1980; Ayling et al., 1995; Zong et al., 2016), as illustrated in Fig. 5c.

$$\left. \begin{aligned} a_{1r} &= 0.513 \\ a_{2r} &= 0.03442/f_c = 5.624 \times 10^{-4} \text{ MPa}^{-1} \end{aligned} \right\} \quad (34)$$

$$\sigma_r = \frac{p}{0.513 + (0.03442/f_c)p} \quad (p > 0) \quad (35)$$

Finally, σ_{m3} , σ_{y3} , and σ_r were located as depicted in Fig. 5d.

Table 3

Results of the SHPB compression and tension tests.

Test	Strain rate (s ⁻¹)	Dynamic strength, f_{cd} or f_{td} (MPa)	f_{cd}/f_c or f_{td}/f_t
Compression	71.1	82.01	1.34
	74.6	89.96	1.47
	81.1	93.63	1.53
	102.6	102.2	1.67
	20.4	8.97	1.53
	23.4	9.31	1.59
Tension	25.7	11.04	1.89
	31.8	12.3	2.11
	34.3	13.22	2.26
	38.6	13.78	2.36
	58.6	14.95	2.56
	84.3	16.79	2.88

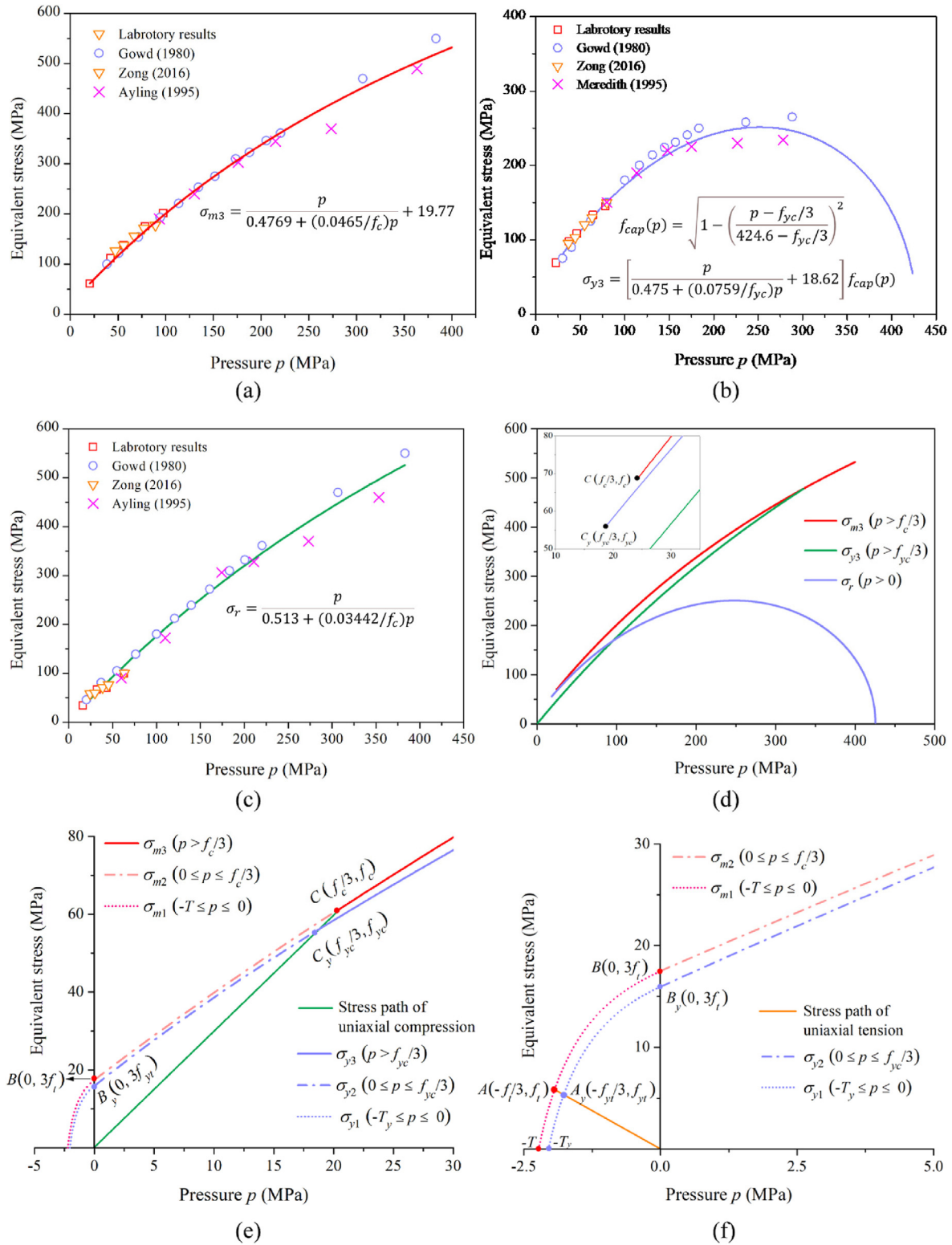


Fig. 5. Calibration of the strength-model-related parameters.

4.1.2. Determination of σ_{m2} and σ_{y2}

After calibrating σ_{m3} , the parameters related to σ_{m2} can be obtained according to the conditions of smoothness and continuity at the connecting point $C(f_c/3, f_c)$ in Fig. 5e:

$$\left. \begin{aligned} \sigma'_{m2}\left(\frac{f_c}{3}\right) &= \sigma'_{m3}\left(\frac{f_c}{3}\right) \\ \sigma_{m2}\left(\frac{f_c}{3}\right) &= f_c \end{aligned} \right\} \quad (36)$$

Substituting the equations of σ_{m2} and σ_{m3} (in Eq. (1)), we obtain a_{1m2} and a_{2m2} as

$$\left. \begin{aligned} a_{1m2} &= \frac{a_{1m3}}{(a_{1m3} + a_{2m3}f_c/3)^2} \left(\frac{f_c/3}{f_c - 3f_t} \right)^2 \\ a_{2m2} &= \left(\frac{f_c/3}{f_c - 3f_t} - a_{1m2} \right) \frac{1}{f_c/3} \end{aligned} \right\} \quad (37)$$

$$\left. \begin{aligned} a_{1m2} &= 0.4285 \\ a_{2m2} &= 0.1146/f_c = 0.001873 \text{ MPa}^{-1} \end{aligned} \right\} \quad (38)$$

Therefore, σ_{m2} can be determined as

$$\sigma_{m2} = \frac{p}{0.4285 + \left(\frac{0.1146}{f_c} \right) p} + 17.49 \text{ MPa} \quad \left(0 \leq p < \frac{f_c}{3} \right) \quad (39)$$

Similarly, a_{1y2} and a_{2y2} are

$$\left. \begin{aligned} a_{1y2} &= \frac{a_{1y3}}{(a_{1y3} + a_{2y3}f_c/3)^2} \left(\frac{f_{yc}/3}{f_{yc} - 3f_{yt}} \right)^2 \\ a_{2y2} &= \left(\frac{f_{yc}/3}{f_{yc} - 3f_{yt}} - a_{1y2} \right) \frac{1}{f_{yc}/3} \end{aligned} \right\} \quad (40)$$

$$\left. \begin{aligned} a_{1y2} &= 0.341 \\ a_{2y2} &= 0.3773/f_{yc} = 6.76 \times 10^{-3} \text{ MPa}^{-1} \end{aligned} \right\} \quad (41)$$

Then, σ_{y2} can be determined as

$$\sigma_{y2} = \frac{p}{0.341 + \left(\frac{0.3773}{f_{yc}} \right) p} + 15.95 \text{ MPa} \quad \left(0 \leq p < \frac{f_{yc}}{3} \right) \quad (42)$$

4.1.3. Determination of σ_{m1} and σ_{y1}

As shown in Fig. 5f, σ_{m1} was located by the tensile cutoff $(-T, 0)$, $A(-f_t/3, f_t)$, $B(0, 3f_t)$, and the smoothness condition at B as follows:

$$\left. \begin{aligned} \sigma'_{m1}(0) &= \sigma'_{m2}(0) \\ \sigma_{m1}(0) &= 3f_t \\ \sigma_{m1}(-f_t/3) &= f_t \end{aligned} \right\} \quad (43)$$

a_{1m1} , a_{2m1} , and T can be expressed as

$$\left. \begin{aligned} a_{1m1} &= \frac{2a_{1m2}}{18a_{1m2} - 1} \\ a_{2m1} &= \left(1 - \frac{a_{1m1}}{a_{1m2}} \right) \frac{1}{3f_t} \\ T &= 3f_t a_{1m1} \end{aligned} \right\} \quad (44)$$

$$\left. \begin{aligned} a_{1m1} &= 0.1277 \\ a_{2m1} &= 0.234/f_t = 0.04014 \text{ MPa}^{-1} \\ T &= 2.23 \text{ MPa} \end{aligned} \right\} \quad (45)$$

Thus, σ_{m1} is determined as

$$\sigma_{m1} = \frac{p + 2.23 \text{ MPa}}{0.1277 + \frac{0.234}{f_t}} \quad (p < 0) \quad (46)$$

Similarly, a_{1y1} , a_{2y1} , and T_y can be obtained as

$$\left. \begin{aligned} a_{1y1} &= \frac{2a_{1y2}}{18a_{1y2} - 1} \\ a_{2y1} &= \left(1 - \frac{a_{1y1}}{a_{1y2}} \right) \frac{1}{3f_{yt}} \\ T_y &= 3f_{yt} a_{1y1} \end{aligned} \right\} \quad (47)$$

$$\left. \begin{aligned} a_{1y1} &= 0.133 \\ a_{2y1} &= 0.203/f_{yt} = 0.0382 \text{ MPa}^{-1} \\ T_y &= 2.12 \text{ MPa} \end{aligned} \right\} \quad (48)$$

Finally, σ_{y1} is

$$\sigma_{y1} = \frac{p + 2.12 \text{ MPa}}{0.133 + \frac{0.203}{f_{yt}}} \quad (p < 0) \quad (49)$$

4.2. Calibration of the equation of state

To obtain the $p - \mu_v$ data to calibrate the EOS, two types of approaches can be employed: conventional non-hydrostatic TXC tests and hydrostatic compression tests. For the first type, relatively more pressure loads are required due to the existing shear deformation and less lateral constraint compared to the second type. Thus, the pressure at the same volumetric strain measured using conventional non-hydrostatic TXC tests is larger than the pressure measured by hydrostatic compressive tests, even for the same sample. However, under high pressure, the material is compacted into a plastic body with continuous, isopycnic, and quasi-static states. Therefore, in the conventional TXC tests under high pressure, the rock can be considered an isobaric body even in the non-hydrostatic conditions, where the $p - \mu_v$ data are identical with those in hydrostatic compressive tests. In addition, there are significantly more existing conventional non-hydrostatic TXC test data than hydrostatic compression tests. Consequently, the conventional non-hydrostatic TXC test data can be used to calibrate the EOS in this paper.

As depicted in Fig. 6, a three-part $p - \mu_v$ curve was adopted. The first region (I) was defined as a linear-elastic region with an upper limit of the uniaxial compressive yield strength ($\mu_{yc} f_{yc}/3$). Actually, region I is nonlinear due to the closure of flaws and pores nearby. Herein, the linear-elastic simplification was adopted because region I has a small effective range and the nonlinear characteristics in region I and the other regions cannot be simultaneously and precisely described by a cubic polynomial in Eq. (9). The yield volumetric strain under uniaxial compression μ_{yc} is calculated in the frame of elastic mechanics:

$$\mu_{yc} = \frac{p_{yc}}{K_{el}} = \frac{f_{yc}/3}{E_0/[3(1 - 2\nu)]} \quad (50)$$

where E_0 is the elastic modulus under uniaxial compression.

For the loading condition, regions II and III have an identical equation to Eq. (9). To ensure that the EOS of Eq. (9) crosses the point $(\mu_{yc} f_{yc}/3)$, Eq. (9) was modified as follows:

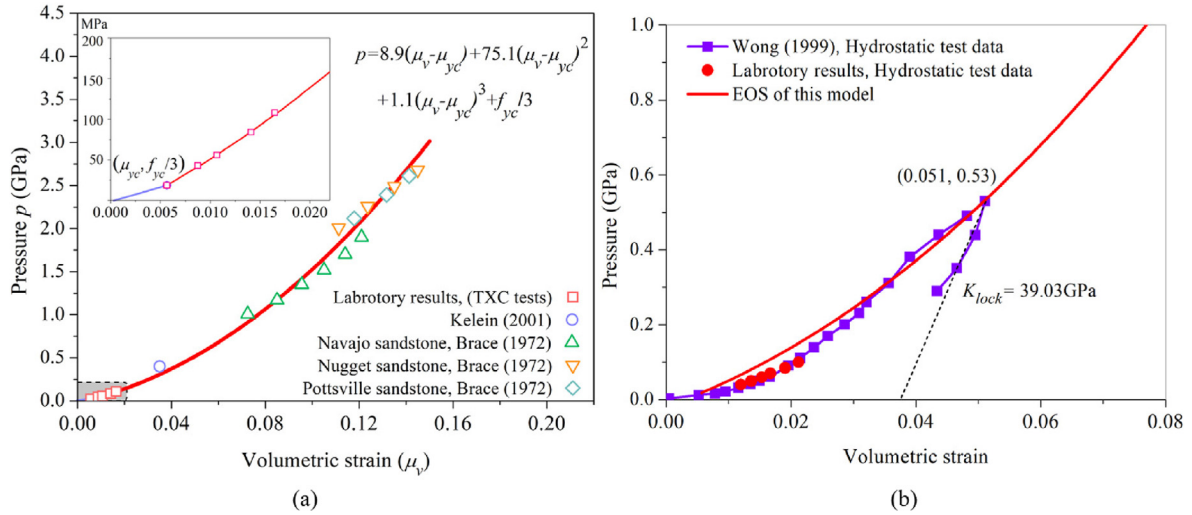


Fig. 6. Determination of the EOS and lock-point-related parameters.

$$p(\mu) = K_1(\mu_v - \mu_{yc}) + K_2(\mu_v - \mu_{yc})^2 + K_3(\mu_v - \mu_{yc})^3 + f_{yc}/3 \quad (51)$$

A large quantity of $p - \mu_v$ data at the peak strengths of TXC tests in this paper (in Fig. 2) and previous research (Brace and Riley, 1972; Klein et al., 2001) were collected in Fig. 6a. The parameters of Eq. (51) can be obtained based on these experimental data as follows: $K_1 = 8.9$ GPa, $K_2 = 75.1$ GPa, $K_3 = 1.1$ GPa.

The EOS of regions II and III was determined as

$$p(\mu) = 8.9(\mu_v - \mu_{yc}) + 75.1(\mu_v - \mu_{yc})^2 + 1.1(\mu_v - \mu_{yc})^3 + f_{yc}/3 \quad (52)$$

In addition, the lock point parameters (μ_{lock}, p_{lock}) and unloading bulk modulus K_{lock} at the point should be calibrated to calculate the current unloading/reloading bulk modulus (in Eq. (11)) in the computational code. Cyclic loading/unloading data under high hydrostatic pressure are required to determine the lock point parameters. However, there are no available cyclic hydrostatic test data for the sandstone specimen with similar properties as the sandstone in this paper. Only a set of previous hydrostatic compression test result (Wong and Baud, 1999) with one unloading can be used, as listed in Fig. 6b, with consistency with the low-pressure test data of this paper, as depicted in Fig. 6b.

To overcome the limitation of available experimental data, we suggest replacing p_{lock} with p_{close} of σ_{y3} in Eqs. (2), (32) and (33). The feasibility of this simplification is as follows: as the pressure where the initial yield strength is nearly zero, p_{close} is the demarcation point of the uncompacted and compacted state of pores and flaws. This demarcation point also appertains to the effect of the locked pressure p_{lock} in the EOS. Thus, p_{close} can be considered a substitute for p_{lock} if little cyclic hydrostatic test data are available, but adequate TXC test data can be adopted to determine p_{close} .

Then, μ_{lock} can be given as 0.04091 by substituting the determined p_{lock} into the calibrated EOS of Eq. (52). The maximum unloading bulk modulus $K_{lock} = 39.03$ GPa can be obtained because the locked pressure is lower than the unloading pressure of the experimental result of Wong et al. (Wong and Baud, 1999), as illustrated in Fig. 6b. Finally, the locked parameters are determined

as follows: $\mu_{lock} = 0.04091$, $p_{lock} = p_{close} = 424.6$ MPa, $K_{lock} = 39.03$ GPa.

4.3. Calibration of the strain-rate effect

To determine the strain rate formulae of Eqs. (15) and (16), SHPB tests with a strain-rate range of $10\text{--}100 \text{ s}^{-1}$ were conducted, as listed in Table 3. Moreover, several dynamic test results at higher and lower strain rates were adopted from previous tests (Liu et al., 2012; Alam et al., 2015; Mishra et al., 2017; Fakhimi et al., 2018; Wicaksana et al., 2018; Gong et al., 2019; Mishra et al., 2019; Majedi et al., 2020; Dong et al., 2021) for more precise DIF_s and DIF_t , as shown in Fig. 7.

There is a sensitive region with much stronger strain rate sensitivity than other regions. To more accurately fit the used experimental data in the case of tension, V_x^t , V_y^t , and DIF_{max}^t can be used to control the slope of the sensitive region, horizontally move the sensitive region and determine the maximum of DIF_t , respectively, as illustrated in Fig. 7. According to a review research on the DIF formulae for rock strength based on the reported data during the past five decades (Liu et al., 2018), DIF_{max}^s and DIF_{max}^t can be calibrated as 6 and 10, respectively. The other parameters were given by the adapted experimental data, as listed in Table 4. The calibrated DIF curves of Eqs. (15) and (16) are consistent with the test data, as depicted in Fig. 7.

4.4. Calibration of the damage parameters

In the computational code for the damage evolution, damage parameters b_1 and b_2 are first employed to calculate the tensile and shear damage indices in Eq. (20), and PtF , R_t^h and R_s^h are used to calculate the hydrostatic-induced damages in Eqs. (22) and (23). Then, λ_m^i and BtA_i are applied to calculate the damage scale factors $\eta(\lambda)$ in Eq. (25). These damage parameters can be classified into three catalogues of shear, tensile, and hydrostatic damage-related parameters.

The shear- and tension-damage-related parameters should be determined by a numerical-experimental comparison method based on UUC, TXC, and BD tests. R_t^h and R_s^h can be obtained by fitting the residual strength data after hydrostatic compression tests at different hydrostatic pressures. Consequently, R_t^h and R_s^h should be determined before the shear- and tension damage-related parameters. Shear damage-related parameters include b_2 ,

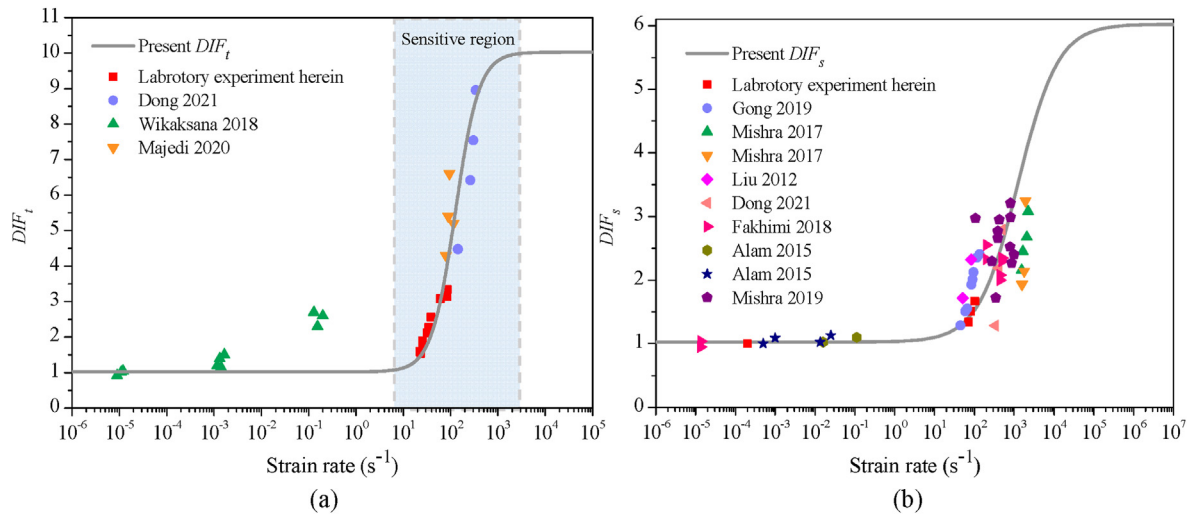


Fig. 7. Determination of (a) DIF_t and (b) DIF_s .

Table 4
Model parameters of the sandstone DIF .

Tension			Shear		
V_x^t	V_y^t	DIF_{max}^t	V_x^s	V_y^s	DIF_{max}^s
2	4.2	10	1	3.1	6

λ_m^s , and BtA_s . Eq. (20) indicates that b_2 is negatively correlated with the shear damage indices. The rising shape and descending slope of the $\eta - \lambda_s$ curve, which define the rates of strain hardening and softening of the sandstone, are controlled by λ_m^s and BtA_s , as represented in Fig. 8. λ_m^s determines the hardening range, while BtA_s determines the softening range. Because λ_m^s and BtA_s have more complex effects than b_2 and the softening range can be expressed by λ_m^s , one should first determine λ_m^s , subsequently BtA_s , and finally b_2 .

Based on the experimental results of Cui et al. (2017), R_s^h , R_t^h , and PtF can be determined as $R_s^h = 0.27$, $R_t^h = -1.05$, and $PtF = 1$ as schematically shown in Fig. 9. λ_m^s , BtA_s , and b_2 were determined by a series of single-element tests. The cube used in single-element tests had a size of 10 mm × 10 mm × 10 mm. The boundary and

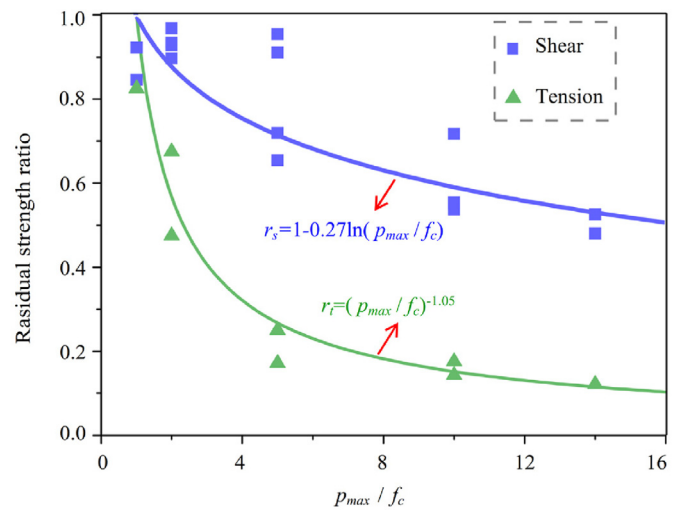


Fig. 9. Residual ratios of the UUT and UUC strengths after the action of different hydrostatic pressures (Cui et al., 2017).

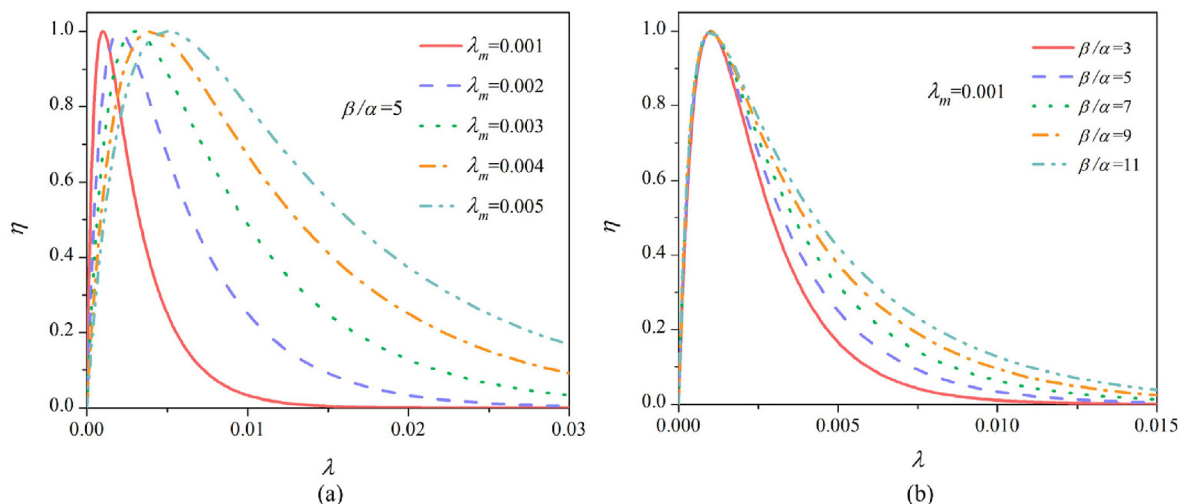


Fig. 8. Influences of (a) λ_m and (b) β/α on scale factor η .

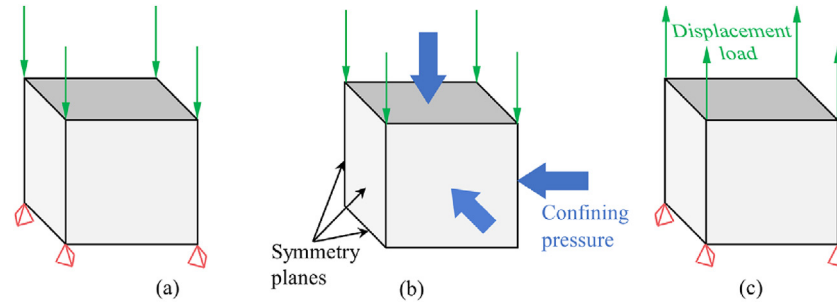


Fig. 10. Single-element tests: (a) UUC, (b) TXC, and (c) UUT.

loading conditions were set according to UUC and TXC tests, as illustrated in Fig. 10.

First, a set of single-element tests of UUC with different λ_m^s was performed with fixed $b_2 = 1$ and $BtA_s = 2$, respectively. The results were compared with the experimental result, as shown in Fig. 11a, where the post-peak softening was fast due to the lack of lateral confining pressure. The hardening range enlarged when λ_m^s increased. To ensure numerical stability, λ_m^s was taken as $\lambda_m^s = 2 \times 10^{-4}$.

Second, a set of single-element tests of TXC ($\sigma_3 = 30$ MPa) with different BtA_s was performed with fixed $b_2 = 1$ and $\lambda_m^s = 2 \times$

10^{-4} . When BtA_s increases, the softening range enlarges and the softening rate decreases, as depicted in Fig. 11b. The experimental result of TXC ($\sigma_3 = 30$ MPa) exhibits a dramatic decline of post-peak softening instead of gradual softening, which is limited by the testing equipment. Based on the TXC ($\sigma_3 = 30$ MPa) result of two experiments (Gowd and Rummel, 1980; Ayling et al., 1995) on sandstone with similar properties, BtA_s was determined as $BtA_s = 2$ to achieve the nearest softening rate to the two existing TXC test results.

Third, b_2 was calibrated by several single-element tests of TXC ($\sigma_3 = 30$ MPa) with fixed $\lambda_m^s = 2 \times 10^{-4}$ and $BtA_s = 2$. The

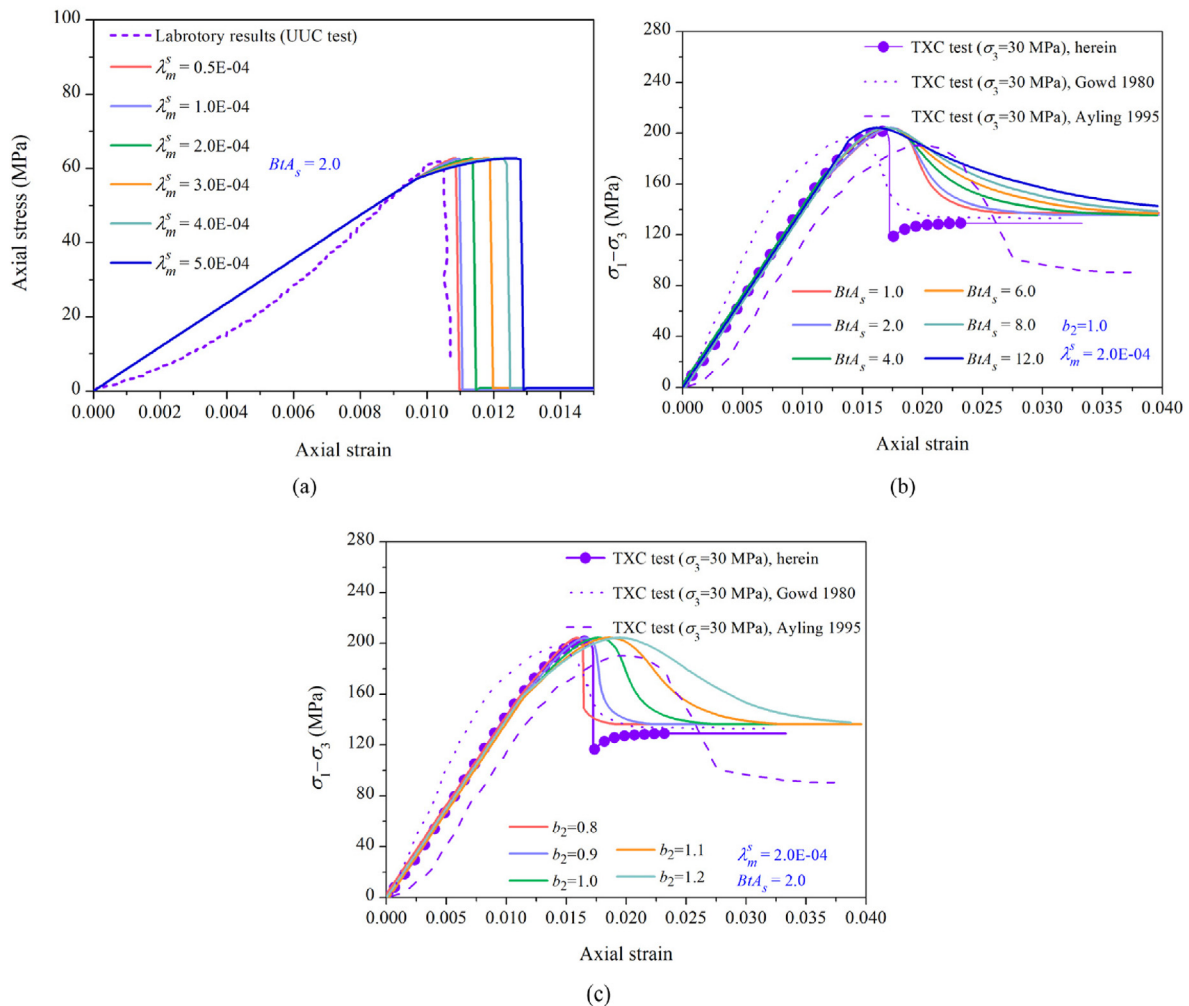


Fig. 11. Influences of the shear damage parameters of (a) λ_m^s , (b) BtA_s , and (c) b_2 on the results of single-element tests.

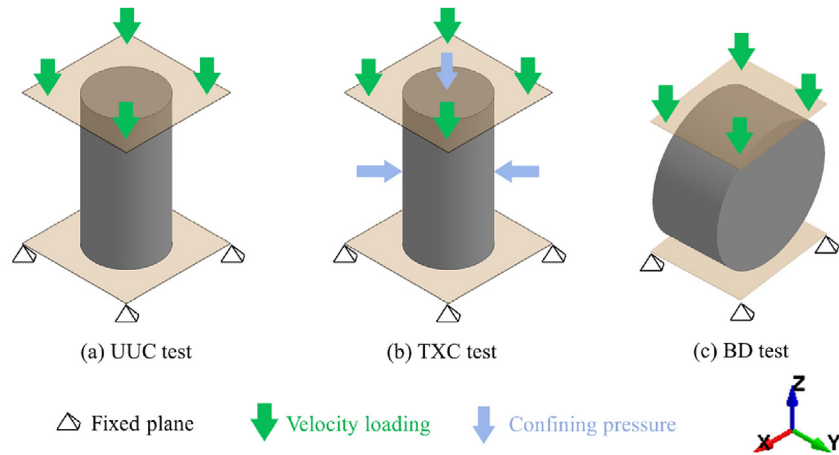


Fig. 13. Boundary conditions for the (a) UUC, (b) TXC, and (c) BD tests.

(diameter \times height: 50 mm \times 100 mm) as the experiments, and the numerical BD test specimen size was 50 mm \times 25 mm (diameter \times height). The mesh sizes for UUC, TXC, and BD tests were 1.75 mm \times 1.75 mm \times 2.5 mm, 1.5 mm \times 1.5 mm \times 2 mm, and 0.95 mm \times 0.95 mm \times 1.05 mm, respectively. Fig. 13 shows the boundary and loading conditions of numerical tests. The rigid bottom wall was fixed, while the top wall only moved in the z-direction. For UUC and BD tests, the z-direction velocity load on the top wall was the only loading condition. In the TXC test, a confining pressure at the assigned value should be applied on the cylinder surface and top wall before the axial velocity load on the top wall. The static friction coefficient was set as 0.56 (Kuciewicz et al., 2020) to prevent the Brazilian disc from rolling. The keyword *DATABASE_BINARY_INTFOR in LS-DYNA was employed to record the

force load histories on the interface between the top wall and the sample. Then, the axial stress-strain curve was obtained from the force on the interface and displacement of the top wall, which is similar to experimental data processing. The parameters in the TSID model for the sandstone were given from the calibrated results in Table 5.

In addition, to validate the effectiveness of the calibrated parameters for high dynamic loads, an SHPB split test and an SHPB compression test in Section 3 were simulated with the calibrated parameters. The numerical models contained an incident bar, a sandstone sample, and a transmission bar with identical geometric sizes as shown in Fig. 14. The rock specimens had a mesh size of 1–2 mm. The mesh size of the bars was set as 4–5 mm, as depicted in Fig. 14. Two experimentally acquired incident waves were applied

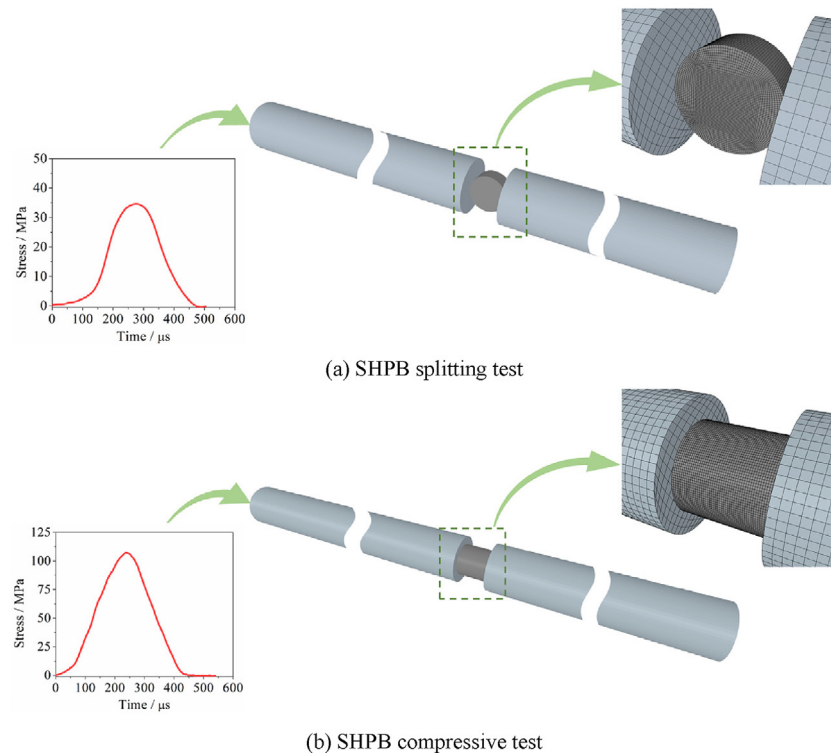
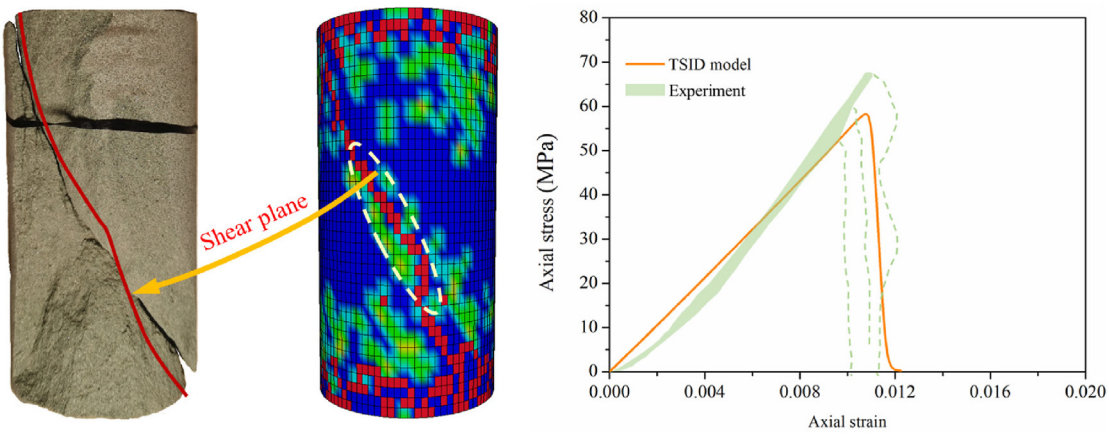
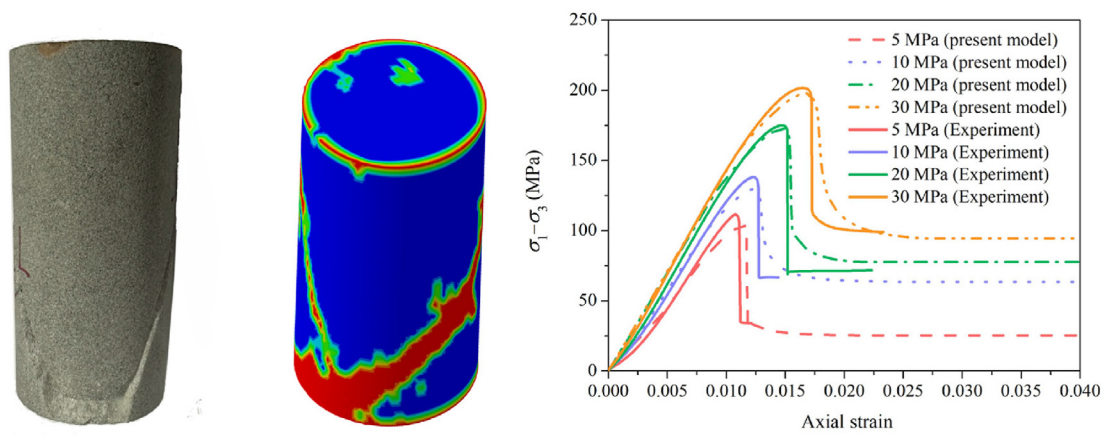


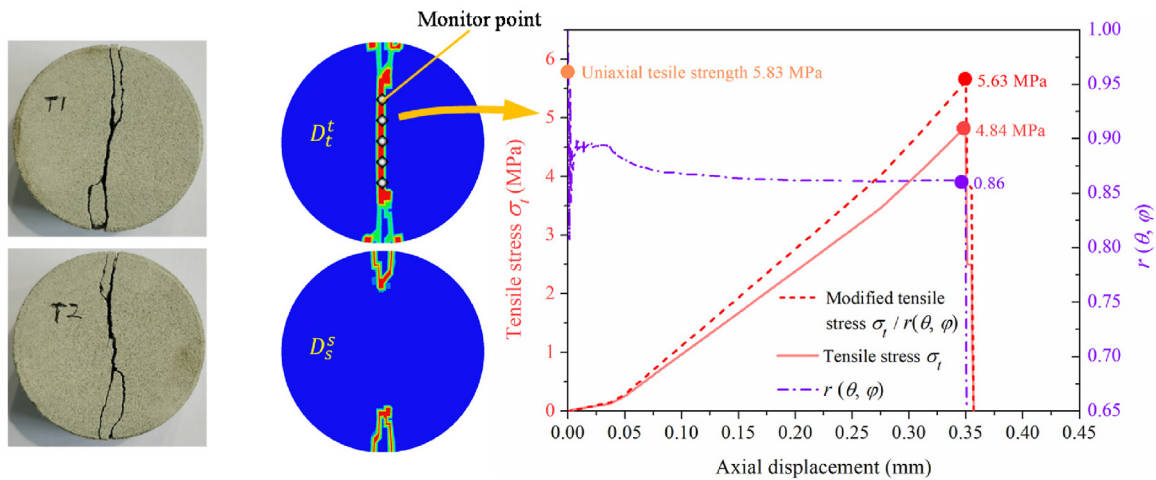
Fig. 14. Numerical model of the SHPB tests.



(a) Simulation results of UUC test



(b) Simulation results of TXC test



(c) Simulation results of BD test

Fig. 15. Simulation results of the (a) UUC test, (b) TXC test, and (c) BD test.

on the end surfaces of the incident bars to replace the striker. As shown in Fig. 14, the maximum peak of the two incident waves is only approximately 110 MPa, much less than the strength of the incident and transmission bars. Thus, selecting the elastic constitutive model for incident and transmission bars is acceptable.

5.2. Numerical test results under static loading

5.2.1. UUC test

Fig. 15a shows the UUC test results predicted by the TSID model. The elements with $D_s = 1$ failed to reproduce a more realistic

fracture mode with a predominant and sloping shear plane. As depicted in Fig. 15a, the numerically simulated shear plane was basically anastomotic with the experiment. Similarly, the axial stress-strain curve and peak strength predicted by the TSID model were near the average of the experimental data. Therefore, the fracture mode and strength characteristics of UUC tests can be precisely reproduced by the TSID model with the calibrated parameters.

5.2.2. TXC test

It is well known that the elastic modulus E increases with confining pressure σ_3 , especially under relatively low confining pressure. To briefly describe the confining pressure effect on the elastic modulus, an empirical relation formula between normalized elastic modulus (E/E_{30}) and normalized confining pressure (σ_3/f_{yc}) was presented based on the experimental results of this paper and previous research (Klein et al., 2001; Zhang et al., 2020). The empirical formula is as follows:

$$\frac{E}{E_{30}} = 1.00005 - 0.57005 \times \left(8.7712 \times 10^{-5}\right)^{\frac{\sigma_3}{f_{yc}}} \quad (53)$$

where E_{30} is the elastic modulus under the confining pressure of 30 MPa, whose value is shown in Tables 2 and 5. The increase in elastic modulus is negligible when the confining pressure σ_3 is

greater than 30 MPa. Thus, the elastic modulus was calculated by Eq. (53) if $\sigma_3 < 30$ MPa, and the elastic modulus was taken as E_{30} if $\sigma_3 \geq 30$ MPa.

Making the confining effect above and Eq. (53) included in the TSID model, the TXC tests under 10 MPa confining pressure were simulated on a complete cylindrical model and a single-element model. Fig. 15b displays the numerical results of the TXC test, which are consistent with the experimental results.

5.2.3. BD test

BD tests have been widely adopted to measure the tensile strength of rock-like materials. Fig. 15c illustrates the tensile damage D_t^I and shear damage D_s^s . The final damage patterns are almost identical to the fracture mode of the experimental results.

In BD tests, the horizontal tensile stress σ_t is commonly given from the axial force load using an indirect method as follows:

$$\sigma_t = \frac{2F_a}{\pi D h} \quad (54)$$

where F_a is the axial force load; and D and h are the diameter and height of the Brazilian disc, respectively.

However, the indirect calculating method is idealized in the elastic mechanics frame, which is inconsistent with the porous condition of the used sandstone. To obtain a more precise

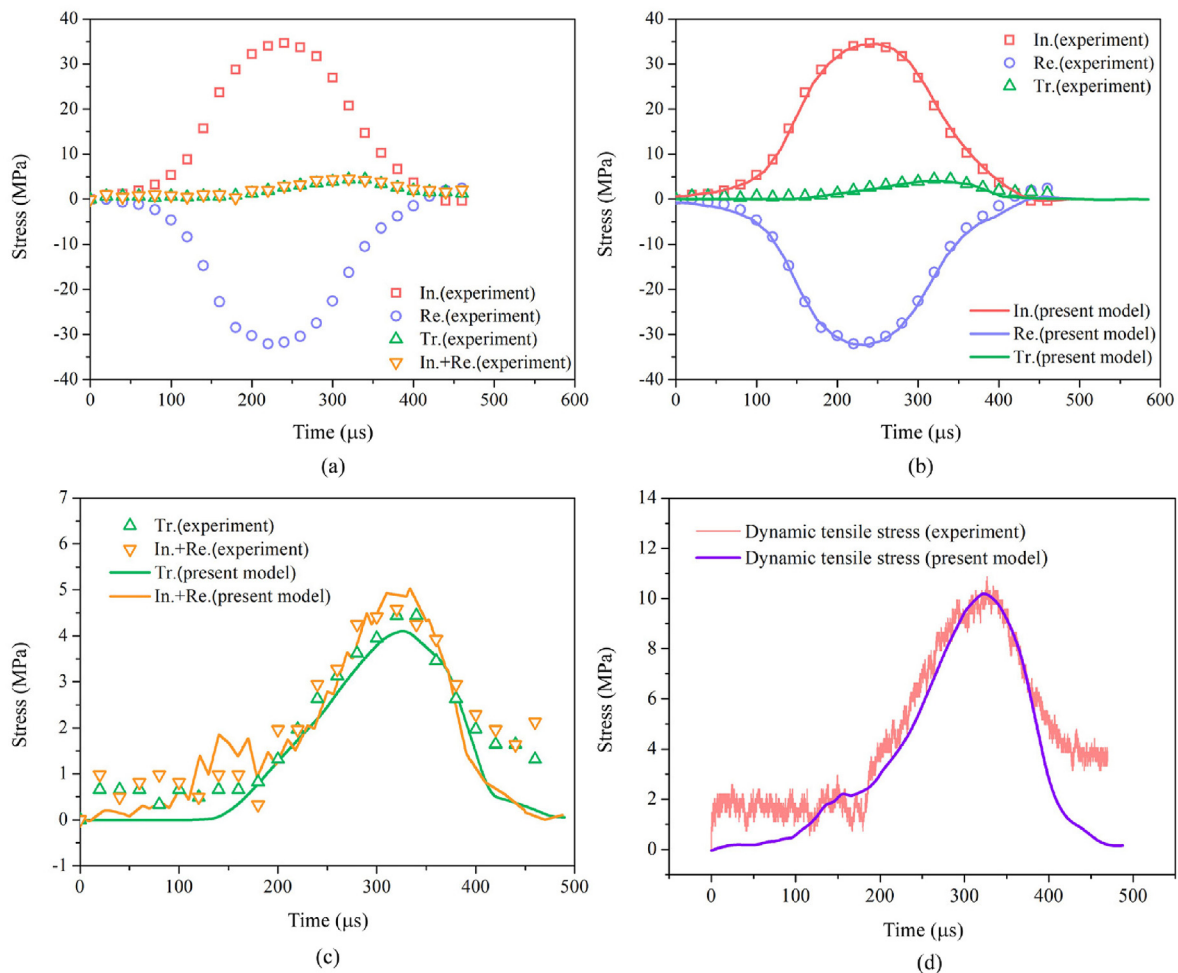


Fig. 16. Comparison of the SHPB split test results between numerical results and experimental data: (a) Dynamic stress equilibrium of experimental data; (b) Incident, transmitted, and reflected waves; (c) Superposition wave; and (d) Dynamic tensile stress.

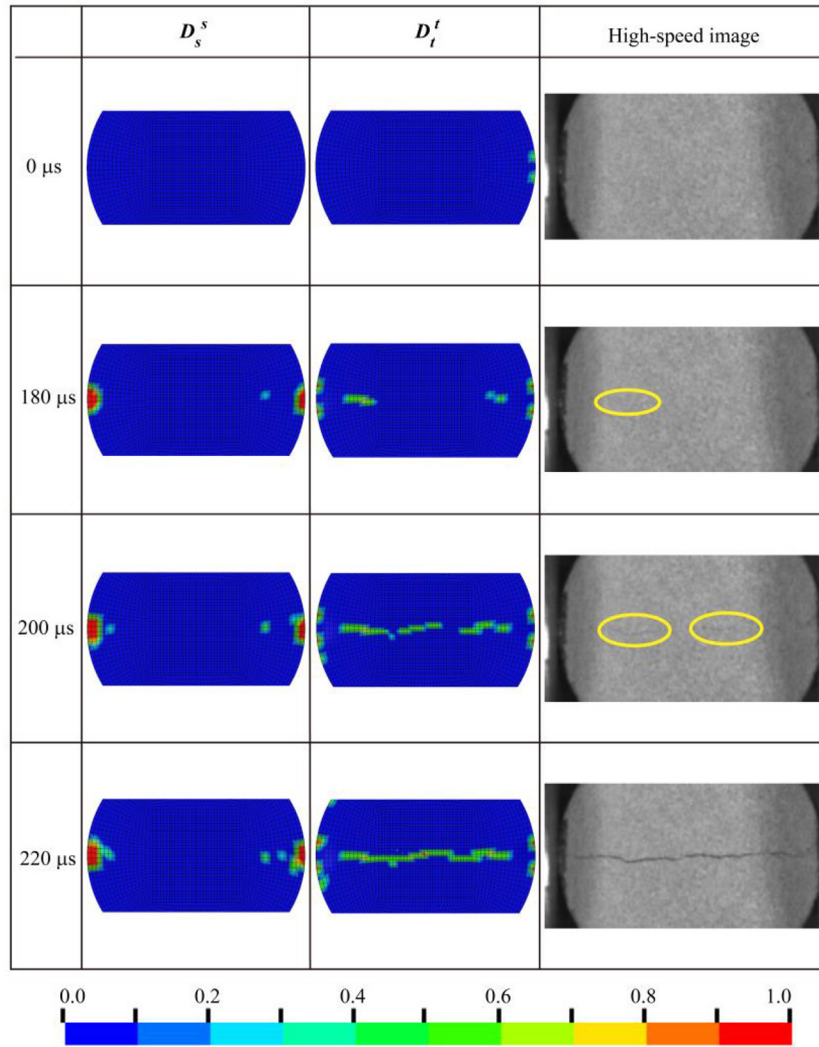


Fig. 17. Comparison of the SHPB split test results between numerical damage pattern and experimental data.

numerical predicted σ_t , five monitors were set at the tensile-damaged elements as depicted in Fig. 15c, and the horizontal stress values at the five monitors were averaged as the numerical predicted σ_t . As shown in Fig. 15c, the peak of σ_t was 4.84 MPa, which is evidently lower than the experimental uniaxial tensile strength (UTS) of 5.83 MPa. The difference is caused by the distinct and complex stress state of the tensile-failure zone in BD tests compared to that in the idealized unconfined direct tensile state. Hence, as the shape function to describe the Lode-angle effect, $r(\theta, \varphi)$ was employed to correct the difference in σ_t due to different stress states. The numerical values of $r(\theta, \varphi)$ at the five monitors were averaged, as illustrated in Fig. 15c. Finally, a modified σ_t was acquired by dividing σ_t by the average $r(\theta, \varphi)$. The peak of the modified σ_t is 5.63 MPa, which is notably close to 5.83 MPa (UTS). The failure mode and tensile strength of standard Brazilian tests for sandstones can be correctly predicted using the proposed TSID model in this work.

5.3. Numerical test results under dynamic loading

5.3.1. SHPB Brazilian disc test

An SHPB Brazilian disc test to determine parameters in Section 3 was first simulated using the calibrated parameters. In Fig. 16, the

incident wave $\sigma_{in}(t)$, transmitted wave $\sigma_{Tr}(t)$, reflected wave $\sigma_{Re}(t)$, and superposition of incident and reflected waves predicted by the TSID model are compared with the experimental data. $\sigma_{in}(t)$, $\sigma_{Tr}(t)$, and $\sigma_{Re}(t)$ from the numerical simulation and experiment were calculated by multiplying the elastic modulus of the bars and the corresponding strain wave $\epsilon_{in}(t)$, $\epsilon_{Tr}(t)$, and $\epsilon_{Re}(t)$, respectively. Fig. 16a indicates that dynamic stress equilibrium was ensured in the loading process. $\sigma_{in}(t)$, $\sigma_{Tr}(t)$, and $\sigma_{Re}(t)$ from numerical prediction were consistent with the experimental data, as illustrated in Fig. 16b and c. To acquire the tensile strength of the Brazilian disc sample, the following equation was used:

$$\sigma_{td}(t) = \frac{2P(t)}{\pi Dh} \quad (55)$$

$$P(t) = \frac{1}{2} A_b E_b [\epsilon_{in}(t) + \epsilon_{Re}(t) + \epsilon_{Tr}(t)] \quad (56)$$

where $\sigma_{td}(t)$ is the dynamic tensile stress of the Brazilian disc sample; $P(t)$ is the loading force history; D and h are the diameter and height of the Brazilian disc, respectively; and A_b and E_b are the cross-sectional area and elastic modulus of bars, respectively.

Dynamic tensile stresses from the simulation and experiment were obtained using Eq. (55) and contrasted with consistency as

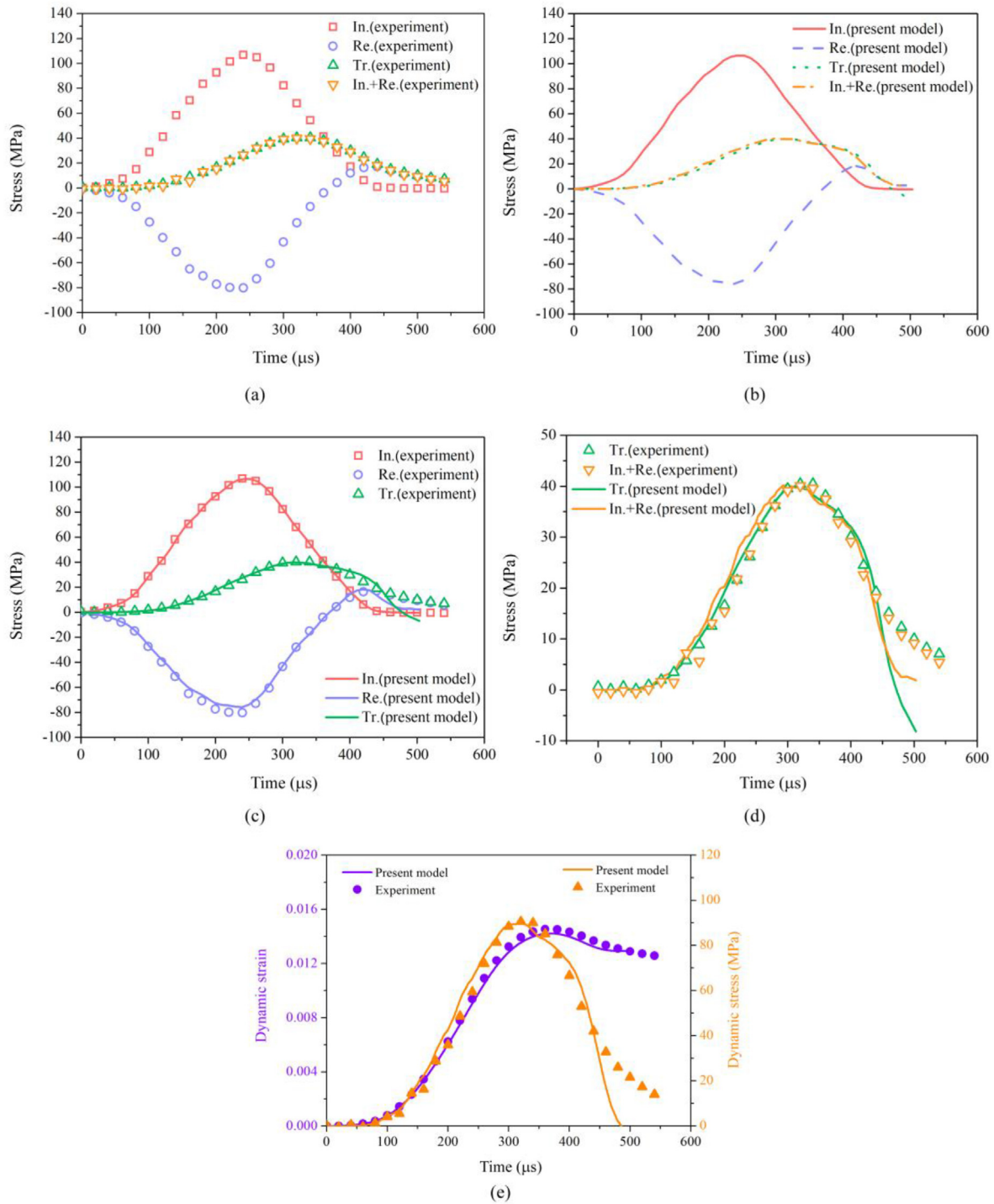


Fig. 18. Comparison of the SHPB compression test results between numerical results and experimental data: (a) Dynamic stress equilibrium of experimental data; (b) Dynamic stress equilibrium of numerical results; (c) Comparison of the incident, transmitted, and reflected waves; (d) Comparison of the superposition wave; and (e) Comparison of the dynamic strain and dynamic stress.

depicted in Fig. 16d. The peak tensile strength and loading rate predicted by the TSID model are consistent with the experimental results.

Finally, the damage states predicted by the TSID model were compared with the fracture pattern captured by the high-speed camera in the experiment, as shown in Fig. 17. The pathway of tensile load-induced tensile damage D_t^I was obviously near the major tensile crack in the center, and the shear load-induced shear

damage D_s^I was limited near the contact points at both ends. It can be proven that the calibrated parameters for the TSID model have excellent performance under dynamic tensile loads.

5.3.2. SHPB compression test

Next, an SHPB compression test with a cylindrical sample in Section 3 was simulated to validate the calibrated parameters. In Fig. 18, the incident wave, transmitted wave, reflected wave and

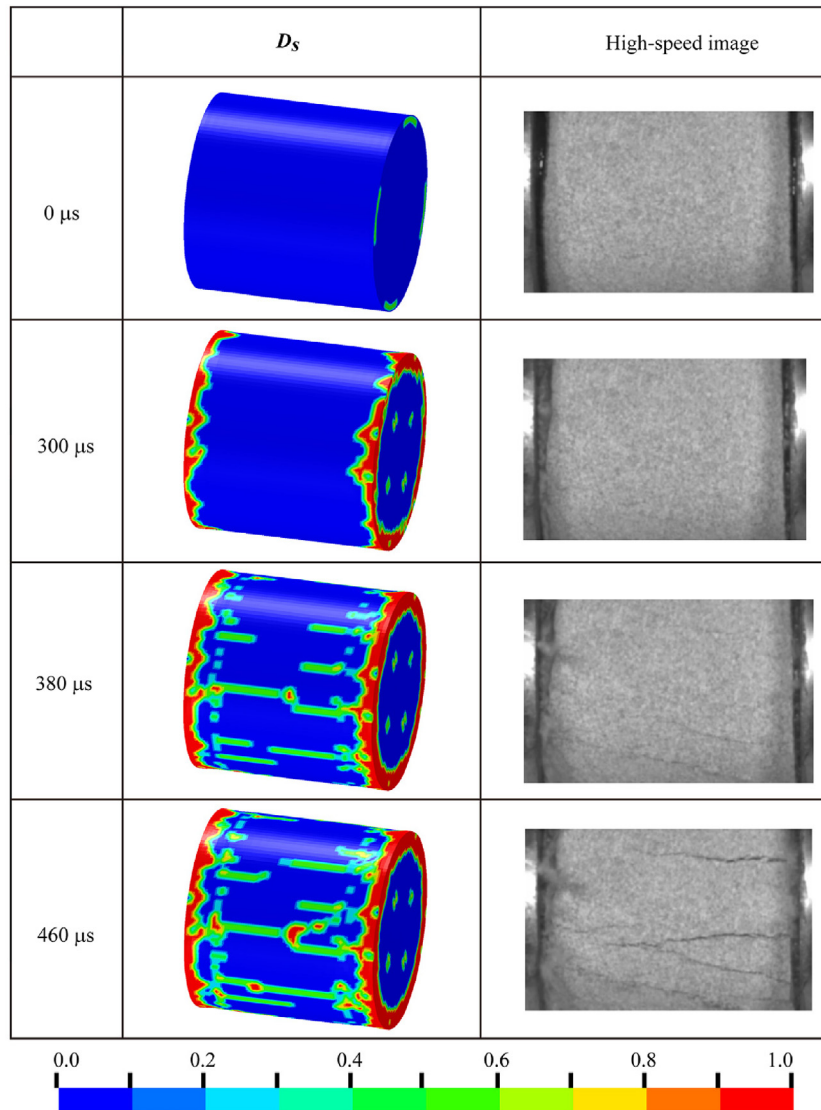


Fig. 19. Comparison of the SHPB compression test results between numerical damage pattern and experimental data.

superposition of incident and reflected waves predicted by the TSID model are compared with the experimental data. Fig. 18a and b indicates that dynamic stress equilibrium was ensured in the experiment and simulation. $\sigma_{In}(t)$, $\sigma_{Tr}(t)$, and $\sigma_{Re}(t)$ from the numerical prediction are consistent with experimental data, as illustrated in Fig. 18c and d. The dynamic axial compressive strain and stress of the specimens were acquired using the following equations:

$$\varepsilon_{cd}(t) = \frac{c_b}{h_s} \int_0^t [\varepsilon_{In}(t) - \varepsilon_{Re}(t) - \varepsilon_{Tr}(t)] dt \quad (57)$$

$$\sigma_{cd}(t) = \frac{A_b E_b}{2A_s} [\varepsilon_{In}(t) + \varepsilon_{Re}(t) + \varepsilon_{Tr}(t)] \quad (58)$$

where $\varepsilon_{cd}(t)$ and $\sigma_{cd}(t)$ are the dynamic compressive strain and stress of the sample, respectively; h_s and A_s are the height and cross-section area of the sample, respectively; and c_b is the elastic wave speed in the bars.

Based on Eqs. (57) and (58), the dynamic strain and stress from numerical simulation were obtained and are consistent with the experimental data, as depicted in Fig. 18e. The dynamic compressive strength, loading rate, and strain rate predicted by the model are consistent with the experimental results. In addition, the shear damage D_s predicted by the TSID model is close to the fracture pattern of experimental high-speed images, as shown in Fig. 19.

The above comparisons demonstrate the satisfactory performance of the calibrated parameters of the TSID model under dynamic loading conditions.

6. Conclusions

A new TSID constitutive model was recently proposed in our previously published work (Shu et al., 2022) that is based on the plastic damage theory for rocks under dynamic impact and blast loads. To present a straightforward and standard parameter calibration procedure of the TSID model, Neijiang sandstone was selected to conduct a series of static and dynamic tests for basic

parameters. Next, the parameter calibration according to a clear order of the strength surface, EOS, strain rate effect, and damage was presented in detail. Notably, the parameters with limited related experimental condition, such as the strength surface parameters based on the smooth continuity condition and the EOS parameters in the high-hydrostatic state, were elaborated on their determination. A widely used *DIF* formula was modified to make fewer parameters with more apparent physics significance. The modified *DIF* formula was separately defined in tension and shear due to the tension-compression asymmetry of the strain-rate effect.

Then, the calibrated parameters were verified by a series of quasi-static numerical tests: UUC, TXC, and BD tests. In addition, SHPB tensile and compressive tests were simulated to validate the dynamic performance of the calibrated parameters and TSID model. The consistency with the experimental data indicates the sound capability and accuracy of the calibrated parameters and TSID model for rock materials.

Declaration of competing interest

The authors declare that they have no known competing financial interests or personal relationships that could have appeared to influence the work reported in this paper.

Acknowledgments

This research was funded by the National Natural Science Foundation of China (Grant No. 12272247), National Key Project (Grant No. GJXM92579), and Major Research and Development Project of Metallurgical Corporation of China Ltd. in the Non-Steel Field (Grant No. 2021-5).

Appendix A. Supplementary data

Supplementary data to this article can be found online at <https://doi.org/10.1016/j.jrmge.2023.08.021>.

References

- Alam, M.S., Chakraborty, T., Matsagar, V., Rao, K.S., Sharma, P., Singh, M., 2015. Characterization of Kota sandstone under different strain rates in uniaxial loading. *Geotech. Geol. Eng.* 33 (1), 143–152.
- Ayling, M.R., Meredith, P.G., Murrell, S.A.F., 1995. Microcracking during triaxial deformation of porous rocks monitored by changes in rock physical properties, i. Elastic-wave propagation measurements on dry rocks. *Tectonophysics* 245 (3), 205–221.
- Brace, W.F., Riley, D.K., 1972. Static uniaxial deformation of 15 rocks to 30 kb. *Int. J. Rock Mech. Min.* 9 (2), 271–288.
- Cui, J., Hao, H., Shi, Y., 2017. Discussion on the suitability of concrete constitutive models for high-rate response predictions of RC structures. *Int. J. Impact Eng.* 106, 202–216.
- Dong, C., Lu, X., Zhao, G., Meng, X., Li, Y., Cheng, X., 2021. Experiment and applications of dynamic constitutive model of tensile and compression damage of sandstones. *Adv. Mater. Sci. Eng.* 2021, 1–13.
- Fakhimi, A., Azhdari, P., Kimberley, J., 2018. Physical and numerical evaluation of rock strength in split Hopkinson pressure bar testing. *Comput. Geotech.* 102, 1–11.
- Gao, W., Zhu, Z., Wang, M., Ying, P., Wang, F., Niu, C., Zhang, X., 2022. Influence of the interlaced holes on crack propagation behavior under impact loads. *Int. J. Impact Eng.* 163, 104178.
- Gebbeken, N., Ruppert, M., 2000. A new material model for concrete in high-dynamic hydrocode simulations. *Arch. Appl. Mech.* 70 (7), 463–478.
- Gharehdash, S., Barzegar, M., Palynskiy, I., Fomin, P., 2020. Blast induced fracture modelling using smoothed particle hydrodynamics. *Int. J. Impact Eng.* 135, 103235.
- Gong, F., Si, X., Li, X., Wang, S., 2019. Dynamic triaxial compression tests on sandstone at high strain rates and low confining pressures with split Hopkinson pressure bar. *Int. J. Rock Mech. Min.* 113, 211–219.
- Gowd, T.N., Rummel, F., 1980. Effect of confining pressure on the fracture behaviour of a porous rock. *Int. J. Rock Mech. Min.* 17 (4), 225–229.
- Holmquist, T.J., Johnson, G.R., 2011. A computational constitutive model for glass subjected to large strains, high strain rates and high pressures. *J. Appl. Mech.* 78 (5), 51003.
- Huang, X., Kong, X., Chen, Z., Fang, Q., 2021. A plastic-damage model for rock-like materials focused on damage mechanisms under high pressure. *Comput. Geotech.* 137, 104263.
- Jiang, M., Chen, H., Crosta, G.B., 2015. Numerical modeling of rock mechanical behavior and fracture propagation by a new bond contact model. *Int. J. Rock Mech. Min.* 78, 175–189.
- Johnson, G.R., Holmquist, T.J., 1999. Response of boron carbide subjected to large strains, high strain rates, and high pressures. *J. Appl. Phys.* 85 (12), 8060–8073.
- Klein, E., Baud, P., Reuschlé, T., Wong, T., 2001. Mechanical behaviour and failure mode of bentheim sandstone under triaxial compression. *Phys. Chem. Earth* 26 (1), 21–25.
- Kong, X., Fang, Q., Chen, L., Wu, H., 2018. A new material model for concrete subjected to intense dynamic loadings. *Int. J. Impact Eng.* 120, 60–78.
- Kuczewicz, M., Baranowski, P., Malachowski, J., 2020. Determination and validation of karagozian-case concrete constitutive model parameters for numerical modeling of dolomite rock. *Int. J. Rock Mech. Min.* 129, 104302.
- Kuczewicz, M., Baranowski, P., Malachowski, J., 2021. Dolomite fracture modeling using the Johnson-Holmquist concrete material model: parameter determination and validation. *J. Rock Mech. Geotech.* 13 (2), 335–350.
- Li, X., Zhu, Z., Wang, M., Wan, D., Zhou, L., Liu, R., 2021a. Numerical study on the behavior of blasting in deep rock masses. *Tunn. Undergr. Space Technol.* 113, 103968.
- Li, X., Zhu, Z., Wang, M., Xiao, D., Shu, Y., Deng, S., 2021b. Fracture mechanism of rock around a tunnel-shaped cavity with interconnected cracks under blasting stress waves. *Int. J. Impact Eng.* 157, 103999.
- Liu, J., Xu, J., Lv, X., Zhao, D., Leng, B., 2012. Experimental study on dynamic mechanical properties of amphibolites, sericite-quartz schist and sandstone under impact loadings. *Int. J. Nonlin. Sci. Num.* 13 (2), 209–217.
- Liu, K., Wu, C., Li, X.B., Li, Q., Fang, J., Liu, J., 2020. A modified HJC model for improved dynamic response of brittle materials under blasting loads. *Comput. Geotech.* 123, 103584.
- Liu, K., Zhang, Q., Zhao, J., 2018. Dynamic increase factors of rock strength. In: *Rock Dynamics and Applications 3*. CRC Press, pp. 169–174.
- Majedi, M.R., Afrazi, M., Fakhimi, A., 2020. A micromechanical model for simulation of rock failure under high strain rate loading. *Int. J. Civ. Eng.* 19 (5), 501–515.
- Malvar, L.J., Crawford, J.E., Wesevich, J.W., Simons, D., 1997. A plasticity concrete material model for DYNA3D. *Int. J. Impact Eng.* 19 (9), 847–873.
- Mishra, S., Chakraborty, T., Basu, D., Lam, N., 2019. Characterization of sandstone for application in blast analysis of tunnel. *Geotech. Test J.* 43 (2), 351–382.
- Mishra, S., Meena, H., Parashar, V., Khetwal, A., Chakraborty, T., Matsagar, V., Chandel, P., Singh, M., 2017. High strain rate response of rocks under dynamic loading using split Hopkinson pressure bar. *Geotech. Geol. Eng.* 36 (1), 531–549.
- Pereira, L.F., Weerheijm, J., Sluys, L.J., 2018. Simulation of compaction and crushing of concrete in ballistic impact with a new damage model. *Int. J. Impact Eng.* 111, 208–221.
- Pittet, C., Lemaître, J., 2000. Mechanical characterization of brushite cements: a mohr circles' approach. *J. Biomed. Mater. Res.* 53 (6), 769–780.
- Polanco-Loria, M., Hopperstad, O.S., Borvik, T., Berstad, T., 2008. Numerical predictions of ballistic limits for concrete slabs using a modified version of the HJC concrete model. *Int. J. Impact Eng.* 35 (5), 290–303.
- Shu, Y., Zhu, Z., Wang, M., Ying, P., Wang, F., Wan, D., Li, X., Gao, W., 2022. A plastic damage constitutive model for rock-like material focusing on the hydrostatic pressure induced damage and the interaction of tensile and shear damages under impact and blast loads. *Comput. Geotech.* 150, 104921.
- Wan, D., Wang, M., Zhu, Z., Wang, F., Zhou, L., Liu, R., Gao, W., Shu, Y., Xiao, H., 2022. Coupled GIMP and CPDI material point method in modelling blast-induced three-dimensional rock fracture. *Int. J. Min. Sci. Technol.* 32 (5), 1097–1114.
- Wan, D., Zhu, Z., Liu, R., Liu, B., Li, J., 2019. Measuring method of dynamic fracture toughness of mode I crack under blasting using a rectangle specimen with a crack and edge notches. *Int. J. Rock Mech. Min.* 123, 104104.
- Wang, Y., Kong, X., Fang, Q., Chen, L., Fan, J., 2021. Modelling damage mechanisms of concrete under high confinement pressure. *Int. J. Impact Eng.* 150, 103815.
- Riedel, W., Thoma, K., Hiermaier, S., Schmolsinske, E., 1999. Penetration of reinforced concrete by beta-b-500 numerical analysis using a new macroscopic concrete model for hydrocodes. In: *Proceedings of ISIEMS, Berlin*, pp. 315–322.
- Wicaksana, Y., Jeon, S., Min, G., Cho, S., 2018. Tensile behavior of rock under intermediate dynamic loading for Hwangdeung granite and Linyi sandstone. In: *Geomechanics and Geodynamics of Rock Masses*. CRC Press.
- Wong, T.F., Baud, P., 1999. Mechanical compaction of porous sandstone. *Oil Gas Sci. Technol.* 54 (6), 715–727.
- Xie, L., Yang, S., Gu, J., Zhang, Q., Lu, W., Jing, H., Wang, Z., 2019. JHR constitutive model for rock under dynamic loads. *Comput. Geotech.* 108, 161–172.
- Xu, H., Wen, H., 2016. A computational constitutive model for concrete subjected to dynamic loadings. *Int. J. Impact Eng.* 91, 116–125.
- Yang, L., Wang, G., Zhao, G., Shen, L., 2020. A rate- and pressure-dependent damage-plasticity constitutive model for rock. *Int. J. Rock Mech. Min.* 133, 104394.
- Ying, P., Li, W., Zhu, Z., Li, X., Gao, W., Shu, Y., 2022. Influence of impact loading orientations on the mechanical behaviour of rocks around a tunnel. *Int. J. Rock Mech. Min.* 152, 105071.

- Zhang, A., Xie, H., Zhang, R., Ren, L., Zhou, J., Gao, M., Tan, Q., 2021. Dynamic failure behavior of Jinping marble under various preloading conditions corresponding to different depths. *Int. J. Rock Mech. Min.* 148, 104959.
- Zhang, S., Wu, S., Zhang, G., 2020. Strength and deformability of a low-porosity sandstone under true triaxial compression conditions. *Int. J. Rock Mech. Min.* 127, 104204.
- Zhao, T., Crosta, G.B., Liu, Y., 2022. Analysis of slope fracturing under transient earthquake loading by random discrete element method. *Int. J. Rock Mech. Min.* 157, 105171.
- Zhu, Z., Li, Y., Xie, J., Liu, B., 2015. The effect of principal stress orientation on tunnel stability. *Tunn. Undergr. Space Technol.* 49, 279–286.
- Zhu, Z., Mohanty, B., Xie, H., 2007. Numerical investigation of blasting-induced crack initiation and propagation in rocks. *Int. J. Rock Mech. Min.* 44 (3), 412–424.
- Zong, Y., Han, L., Wei, J., Wen, S., 2016. Mechanical and damage evolution properties of sandstone under triaxial compression. *Int. J. Min. Sci. Technol.* 26 (4), 601–607.



Meng Wang obtained his BEng and PhD degrees in Engineering Mechanics from Sichuan University, China, in 2010 and 2015, respectively. His research interests include (1) the mechanism and application of rock dynamic load-induced fracturing (including experiments and numerical analysis); and (2) Numerical calculation methods and software development. He has participated in a large number of Chinese national projects and received multiple awards.